Prawn Trawl Shape due to Flexural Rigidity and Hydrodynamic Forces

By

Cheslav Balash

B.Eng (Hons) Kaliningrad State Technical University, Russia (1999)
M.Eng. Memorial University of Newfoundland, Canada (2008)

Submitted in fulfilment of the requirement for the degree of Doctor of Philosophy at the University of Tasmania

June 2012

Declaration of Originality

"This thesis contains no material which has been accepted for a degree or diploma by the University or any other institution, except by way of background information and duly acknowledged in the thesis, and to the best of the my knowledge and belief no material previously published or written by another person except where due acknowledgement is made in the text of the thesis, nor does the thesis contain any material that infringes copyright."

Abstract

Energy efficiency and ecological sustainability have become vital issues for the Australian and global prawn fisheries. The scientific community and innovative industry operators have introduced fishing gear modifications for drag and unwanted catch reduction. This project has investigated the potential for further drag reduction, focusing on the extent to which prawn net flexural rigidity affects the drag.

A novel experimental technique was developed to quantify flexural rigidity for nets. The concept of the technique was to measure the mesh opening under various loads applied in longitudinal and transverse directions. A relative difference between values showed a resistance of the mesh to bend, and the results were fitted into an existing analytical solution. The geometric parameters of nets were measured applying a digital photogrammetric method.

Four prawn trawls built from the netting being assessed for flexural rigidity were examined in a flume tank for drag and shape over a range of velocities. A stereo-vision system was developed to acquire the 3D shape image. The net flexural rigidity and drag showed a piece-wise linear relationship. Another main finding was that the drag coefficient was weakly dependent on the Reynolds number in the typical range for prawn trawl regimes of *1000<Re<1700*.

Acknowledgments

Contents

List of Figures

List of Tables

Nomenclature

a	longitudinal dimension of a knot
A_{mesh}	mesh area
A_{out}	image area (outline area)
A_{porous}	porous area of net
b	transverse dimension of a knot
c	circumference
$C_{D[net]}^{out}$	the drag coefficient for the net as a function of the outline area
$C_{D[cyl]}$	drag coefficient for the circular cylinder
E	modulus of elasticity
f	twine bar tension
F_d	drag force
F_{in}	in-pull force
Fr	Froude number
g	acceleration due to gravity,.
I	second moment of inertia
L	characteristic trawl length
m	mesh bar
n	number of meshes
Ne	Newton's number
P	outside mesh perimeter
q	static force generated by rigging
r	radius
Re	Reynolds number
$R\text{-}tex$	linear density of the netting yarn or twine
S_d	netting solidity (bloackage)
T	frameline tension
U	flow velocity
u_x	horizontal hanging coefficient
U_y	Vertical hanging coefficient
α	incident angle between the flow and net
γ^{*}	volumetric weight
v	kinematic viscosity

ρ water density

ϕ half angle between two adjacent twine bars

Chapter 1
Introduction

This chapter highlights engineering challenges that prawn fisheries presently face. The picture is given in an Australian context, but similar difficulties are experienced in other prawn fishery regions of the world. Project objectives and long-term goals are then formulated; followed by the reviews that familiarise the reader with the background of the project:

- An overview of prawn trawl systems is provided along with the reasons for selecting a prawn trawl design as a case study for the current project.
- Shortcomings of the trawl scaling practices are discussed.
- Drag variables specific to prawn and fishing nets and trawls are discussed.

1.1 Current needs for Australian prawn fisheries from an engineering perspective

According to the Australian Fisheries Management Authority (www.afma.gov.au/fisheries/industry), fisheries and aquaculture is the fifth most valuable rural industry in the country, worth over 2 billion dollars annually. The prawn fishery is one of primer contributors to this figure. As can be seen from Fig. 1.1, prawns are caught in the majority of the Australian coastal regions. Recently, however, the industry is becoming of marginal profitability due to the lower cost of imported farmed prawns and fluctuating fuel expenses (ABARE 2008). With these statistics in mind, it is surprising that Clark (2006) reported

that the research of the prawn industry was primarily focused on environmental issues, but not industry efficiency. Recent research within the prawn industry has primarily focused on by-catch reduction, prawn behaviour and effects of prawn trawling on the seabed with little attention given to gear design. However, gear modifications may not only improve fishery profitability, but maximize effects on ecological sustainability.
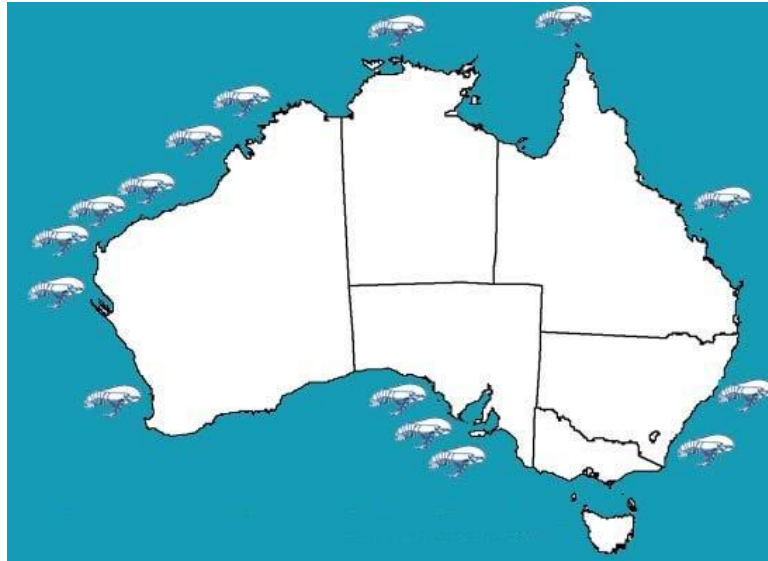
Fig. 1.1 Prawn harvesting in Australia according to the Australian Council for Prawn Fisheries (www.prawncouncil.com.au). Each Australian prawn fishery has been marked with a prawn – it can be seen that prawn fisheries are extended across Australia.

Too often, solutions based on gear modifications are overlooked, and operationally-based changes are implemented instead. This practice impedes the evolution of the gear, and moreover, represents an example of not addressing the source of the problem. For instance, trawl design modifications can greatly reduce the amount of trawl by-catch caught, but the selectivity issue has been seen as largely solved since the introduction of the compulsory use of Turtle Exclusion and By-catch Reduction Devices.

Rising fuel cost, impending oil deficit and global concern for gas emission reduction necessitate improvements of energy efficiency technologies (Sterling, D 2007). The Fisheries Research and Development Corporation (FRDC 2007,

2008) summarised major operational and technical approaches to reduce fuel expenses. Drag force reduction technologies (i.e. skin coatings and naval stabilisers) were suggested as one of the major factors for higher energy efficiency. Fishing gear modification also retains a great potential for drag force reduction. As can be seen from Fig. 1.2, nets and wires can produce up to 2/3 of the total drag whilst trawling.
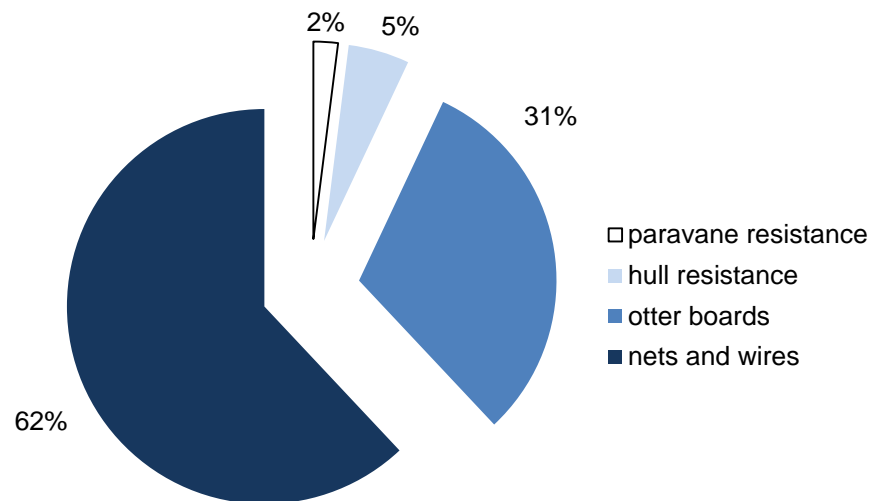
Fig. 1.2 Resistance components of a 22m LWL Success class trawler operating at 3 knots with double-rigged 6 fathom nets (FRDC 2005).

Trawl gear is flexible and its final shape whilst trawling is often unknown. To be able to predict its shape, prior knowledge is required of how inertial, viscous and gravitational forces impact on the load distribution through the net. Once understood better, then these net shape predictions will allow a more detailed assessment of the selectivity and seabed impacts of the net.

The establishment of the relationship between trawl shape and forces may allow the production of a net design with lower water resistance. Such new net modifications should promote better flow throughout the trawl and could inform researchers and off-shore operators for optimal selectivity. In addition, a better knowledge of trawl shape and nearby water flow will enhance trawl gear development and operation, and provide the industry more confidence to participate in gear development processes.

1.2 Aims and goals

The ultimate project goal is to address the issues of trawl selectivity and energy efficiency through designing a prawn trawl of low drag and minimised ecological footprint.

The following major objectives are addressed within this thesis:

- To develop a tool for trawl shape measurement in conjunction with applied loads.
- To develop a method for quantifying fish net flexural rigidity (stiffness), and to estimate flexural rigidity figures for conventional and innovative prawn nets.
- To quantify the extent by which net flexural rigidity affects prawn trawl drag.
- To establish a technique allowing prawn full-scale netting material usage in model experiments.
- To estimate by what extent the Reynolds number, net porosity and an angle of incident flow determine the drag coefficient for nets at a low angle of attack in application to prawn trawls.

The achievement of the above objectives will advance the knowledge of fishing net hydrodynamics, and coupled with practices will provide a methodological foundation for designing an optimal prawn trawl system of minimum drag force and optimal selectivity.

1.3 Overview of prawn trawl systems

Prawn trawl designs

A prawn trawl system (Fig. 1.3) is primarily comprised of top and bottom net panels (and sometimes side panels), otter boards and ground chain. The otter boards and the net are connected by wires (bridles). The main purpose of the otter boards is to provide a desired horizontal trawl opening. The ground chain is attached to the mouth of the bottom panel via short vertical chains at regular intervals (approx. 1m). The ground chain provides seabed contact for the trawl,

and stimulates prawns to jump from the seabed as the trawl is towed through the water. The short vertical connection-chains allow the trawl's bottom net panel to be just clear of the seabed, which minimizes the catch of seabed objects, including sessile benthic animals, and also prevents some net damage.
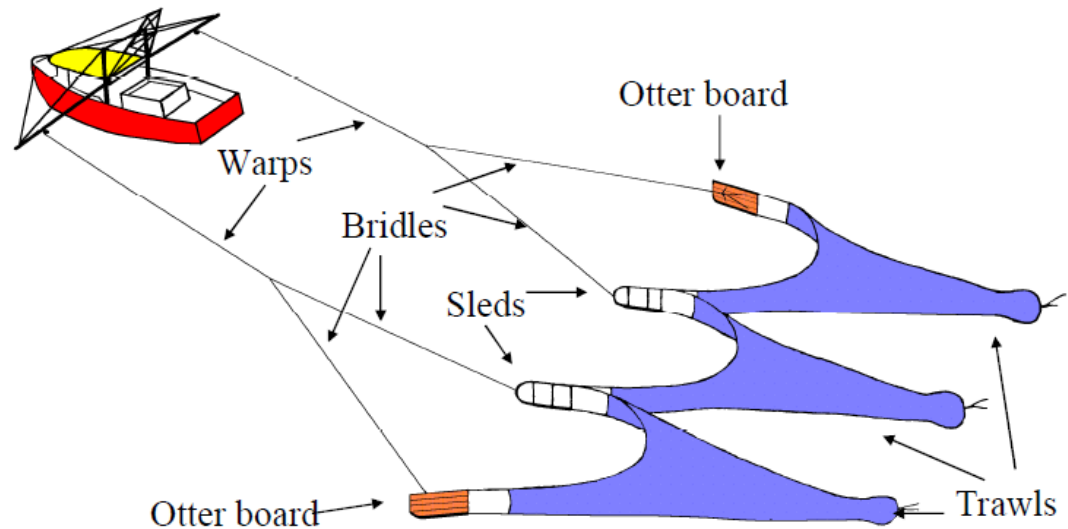
Fig. 1.3 Prawn trawl system components (redrawn from Sterling (1996).

A net plan for a prawn trawl is illustrated in Fig. 1.4. As the panels are symmetric in respect to the trawl's longitudinal centreline, it is common to present only half of the top and bottom panels in the drawing (in this example, the top panel is on the left and bottom panel is on the right). The forepart of the top panel is extended forwards compared to the bottom panel. This 'lead-a-head' feature ensures that prawns are not able to jump vertically over the trawl. The industry employs a variety of net designs. Each net design implies specific sequences of cutting angles, panel sizes and panel combinations (with or without side panels). The cutting angles are achieved by a series of mesh, point and bar cuts, namely tapers. Examples of tapers are shown in Fig. 1.4. The bar is defined as a piece of twine forming one side of a mesh; and the point is a half mesh. The side panels are used if a higher vertical opening of the trawl is desired.

Wing Panels

Side Panel (optional)

Headline/Footline Tapers

Body Taper

Body Panels

Hung Length

Stretched Length

Hanging Ratio = Hung length / Stretched length

Meshes

1P3B Taper

across bundle

Points

1M2B Taper

along bundle

Legislators Mesh Size

Manufacturers Mesh Size

3Bars

1P3B body taper

1Point

3Bars

1M3B wing taper

1Mesh
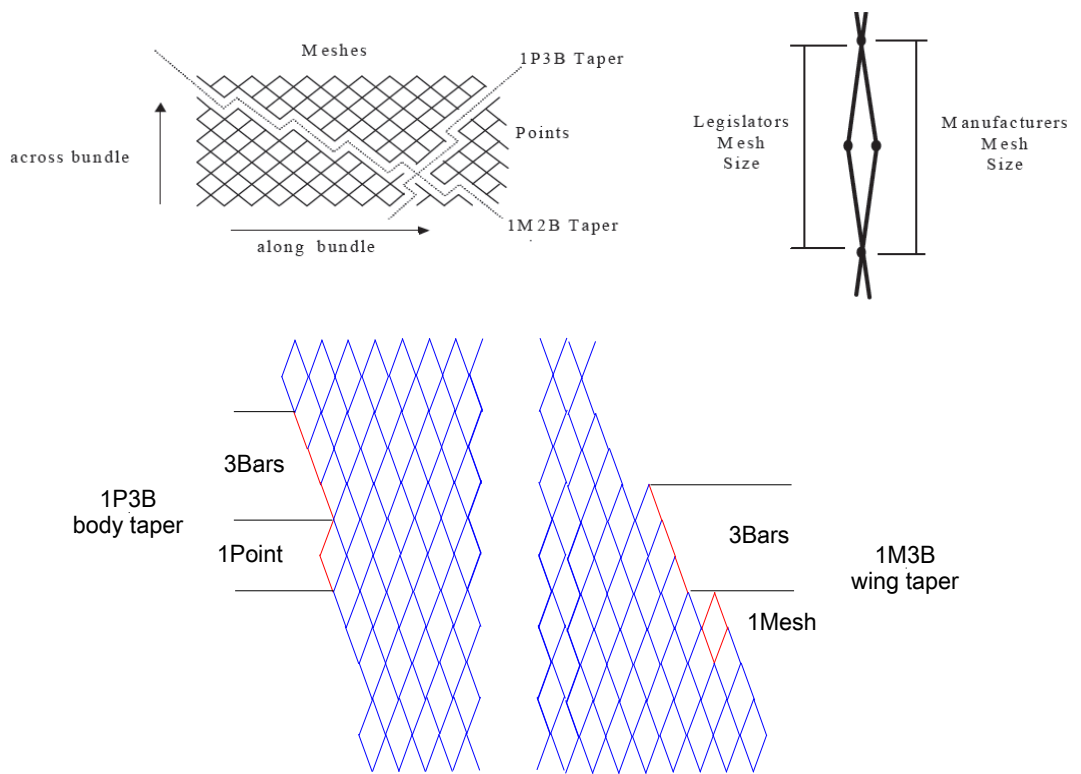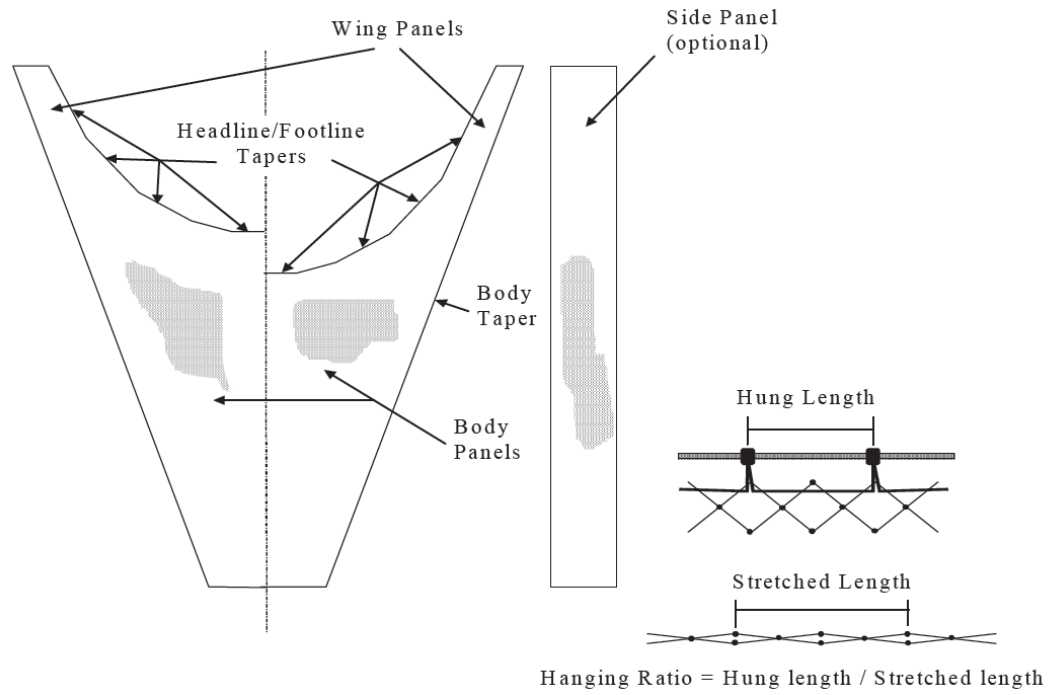
Fig. 1.4 A schematic example of a prawn trawl (above); and examples of body and wing tapers (below). P – Point, M – Mesh, B – Bar. (redrawn from Sterling (1996)

6

Various prawn trawl designs have been developed and utilized across the world. Even within the same country, prawn trawl designs vary from region to region. For example, Watson et al. (1984) conducted a review of various shrimp trawl designs employed in Southeastern United States waters. In Australia four basic designs are most commonly used: Florida Flyer, Sandakan, Gundry and Seibenhauser (Fig. 1.5). Florida Flyer is comprised of a combination of wing tapers, which provides a series of catenaries, while Gundry is typically of one type of a wing taper. Both designs, Florida Flyer and Gundry, often do not have side panels as wide wings provide a high enough vertical trawl opening. Sandakan being a simplified version of Florida Flyer has a lower number of taper sequences in the net mouth, but because of its narrow wings, side panels are required to satisfy the desired vertical trawl opening of about 1m. Seibenhauser has a cut of bars only in the mouth and it is comprised of wide side panels.

Thus, generic features of all four trawls would include:
- A wide wing or a side panel
- A series of two or three wing tapers

As a high horizontal trawl spread is desired for maximum catching performance, it is practical to investigate trawl drag at high spreads only. Wakeford (1994) examined drag variation between the models of Florida Flyer built with different wing tapers: from very steep to shallow. It was shown that in a condition of a high horizontal trawl spread, the drag coefficient between the trawls did not vary greatly. As variation in taper sequences does not significantly affect the drag coefficient for high spreads, a trawl that is comprised of (1) wide wings and (2) cut with tapers of medium steepness can be said to be a generic representative trawl design for Australian prawn fishery. Based on these two major generalisations, an existing 8 fathom Florida Flyer has been modified to create a generic case for the present study. A net plan of this generic case prawn trawl is presented in Fig. 4.1.

a sequence
of wing tapers

no side panels,
but wings
are wider

with side panels and
wings are shallow

FLORIDA FLYER

SANDAKAN

a steep
wing taper

no side panels,
but wings
are wider

wide side panel

a cut of bars only
across the mouth

GUNDRY

SEIBENHAUSER
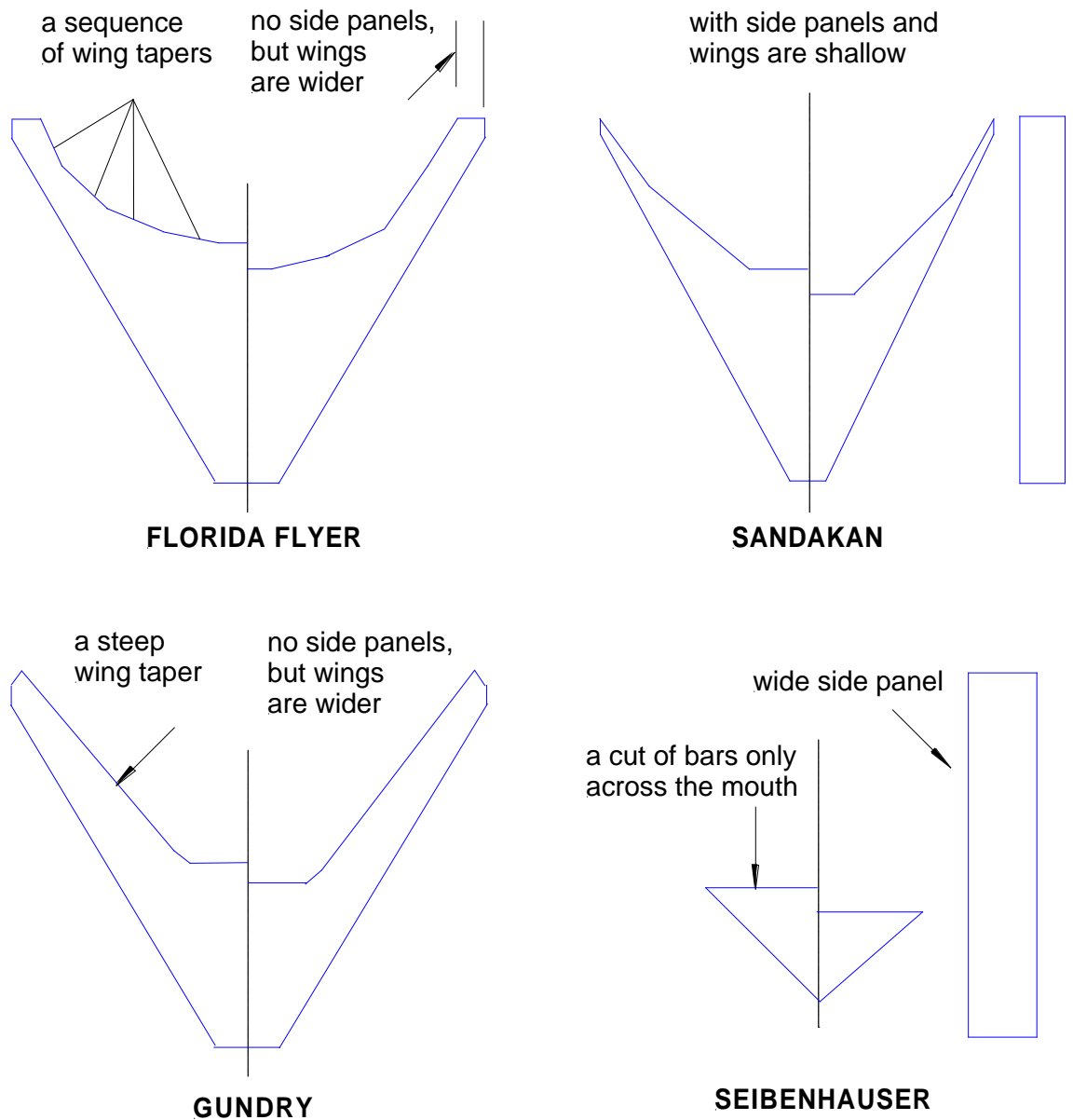
Fig. 1.5 Four prawn net designs traditionally used by trawl operators in
Australia.

Drag saving technologies

A revolutionary drag saving technology was introduced in the Gulf of Mexico in
the early 1950's with a concept of multiple rigs (Fig. 1.6). As can be seen from
Fig. 1.6, a corner stone of the concept is to reduce twine area while keeping a
catching span constant. Initially it was assumed that reducing twine area by 50%
would result in a 50% drag reduction. However, the twine removed from the aft
part of the trawl where netting is exposed at a significantly lower angle to the
flow compared to the wing part, and hence an actual drag decrease is not

linearly correlated with twine area reduction. Sterling (1996) showed that a triple rig provides about a 50% drag reduction compared to the single rig. The nature of drag saving produced with multiple rigs is not solely due to twine area reduction but due to redistribution of the otter board drag required to spread the trawl. In addition to the double and triple rigs shown in Fig. 1.6, the industry also employs quad and five rigs. However, besides drag saving benefits, fishermen need to consider operational implications of using multiple rigs. For example, as the quad rig is a system of two independent double rigs, uneven gear tension distribution caused by the rough sea-bed are more likely to occur while trawling the quad rig, which may lead to netting damage or even to the vessel being capsized.

A more recent innovation to significantly reduce drag was high-strength Dyneema® and spectra netting materials that allow the use of thinner twine compared to traditional materials. Small diameter Dyneema® and spectra netting twine are of similar breaking strength to traditional material, but the thinner twine results in decreased drag. However, a disadvantage of the new material is that it is significantly more expensive than the conventional netting, which makes trawl operators reluctant to widely implement the innovation. In addition, Dyneema® twine has very low bending stiffness, which produces operational difficulties due to fouling during trawl deployment and hauling.

A pleated-panel trawl built with square-mesh orientation in the side sections (described by Wray (1990) requires less force to spread the trawl as the tension is distributed more directly through the trawl along the square-mesh bars to the otter boards as opposed to a conventional diamond orientation where the tension tends to run to the bosom of the trawl and then to the otter boards along the frame lines. However, for a pleated trawl, a greater amount of twine is perpendicular to the flow because of its mesh orientation, which increases the netting drag and hence negates the benefits of a lower in-pull force.

Some trawl operators across Australia employ a tongue trawl design (Fig. 1.7). A double-tongue trawl design has recently been suggested as a possible new step in achieving drag savings (Sterling & Eayrs 2010), and particularly when using

square-mesh orientation in the top and bottom panels of the trawl, but not in side sections as in the pleated trawl. The square mesh panels are expected to focus the tension in the trawl towards the tongues, and ease the load on the otter boards, hence making the trawl easier to spread and minimise drag as smaller otter boards would be required.

single 24 fathom net

single trawl

2 x 12 fathom double rig

double rig - 50% of twine reduction

3 x 8 fathom triple rig

triple rig - 67% of twine reduction
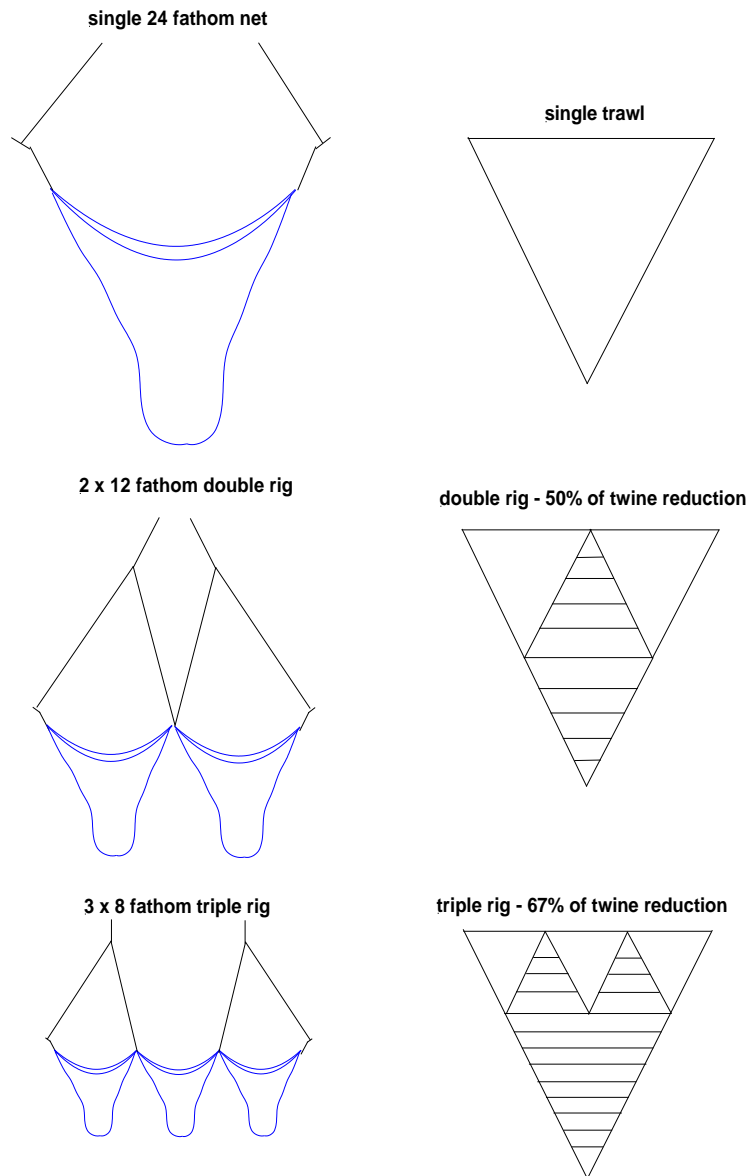
Fig. 1.6 Schematic illustration of twine area reduction for double and triple rigs; a similar situation occurs for quad and quintuple rigs.
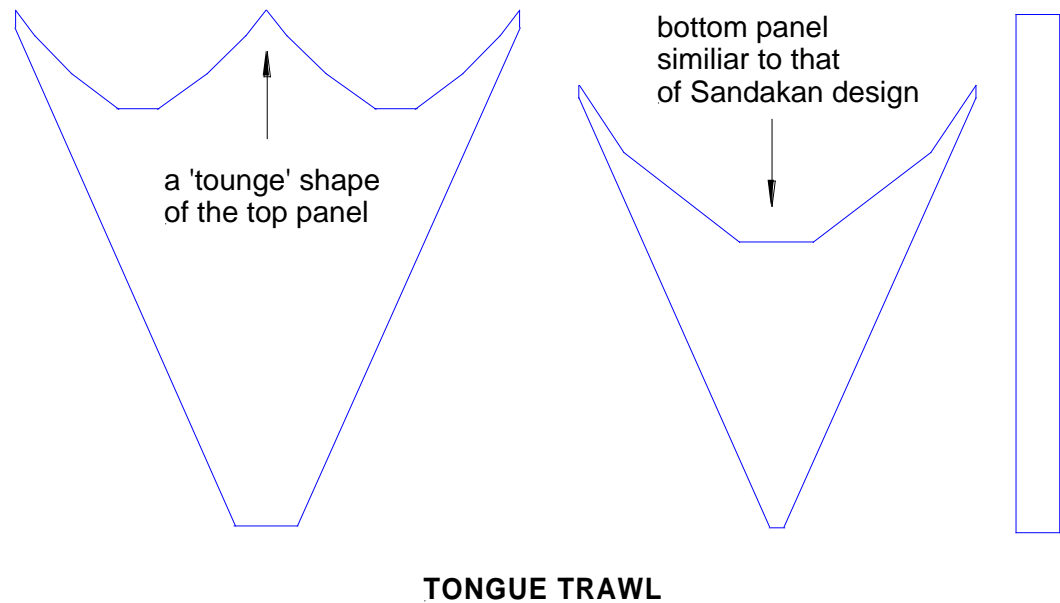
Fig. 1.7 Tongue prawn trawl design.

1.4 Overview of trawl modelling practices

To study a physical phenomenon, analytical, numerical and experimental methods are applied. In application to fishing gear, due to hydro-elastic coupling, establishing and solving equations are possible for simplified cases only (Rozenshtein 2000).

An experimental study can be conducted at model or full-scale. Full-scale experiments at sea ensure the inclusion of all factors influencing the process. However, every run is impacted by secondary factors which are uncontrolled and arbitrary (currents, waves, wind, and uneven sea-bed). In model experiments, a studied process commonly has to be simplified with certain assumptions which may produce an error. However, the model experiments eliminate the noise effect of the environment and they are also more economical.

Initially a relation between experiments at model and full-scale was suggested by Tauti (1934). According to his theory, the drag force is assumed to be proportional to the square of the water velocity U (eq. 1.1):

$$Drag \sim U^2 \qquad\qquad 1.1$$

Chow (1969) and Hu et al. (2001) applied the law to model mid-water trawls at a number of scales. The comparisons with full-scale showed a 50-70% drag force over prediction. The modelling rules were modified; however, those modifications are only applicable for the specific case studied. Fiorenti et al. (2004) also applied Tauti's law for bottom trawls and found a large difference in drag between full-scale and model values. When Tauti's law is applied for model testing, a high drag over prediction occurs as the drag coefficient is assumed to be constant between the model and prototype while it is often not the case.

Dikson (1961) proposed to use the Froude number for scaling:

$$Fr = \frac{U}{\sqrt{gL}}$$
1.2

where U is the flow velocity, g is the acceleration due to gravity, and L is a characteristic trawl length.

A recent application of Dickson's approach (Hu et al. 2001) showed a significant divergence in the drag force between full-scale and model values as for Tauti's method. Applying the Froude number as a condition of dynamic similarity assumes that the net is a solid three-dimensional body, but it is a porous two-dimensional surface (O'Neill, F.G. 2003). Instead O'Neill proposed to use twine thickness d, not trawl length L, as a geometric parameter for the Froude number; and the Reynolds number incorporated the trawl length. It was modified as follows to satisfy the similarity between inertial and viscous forces:

$$R_e = \frac{Ud^2}{\nu L}$$
1.3

where ν is the kinematic viscosity of the water.

Fridman (1973) conducted a dimensional analysis and recommended similarity criteria for fishing gear. The Froude number was modified as a ratio of the hydrodynamic forces to buoyancy forces:

$$Fr = \frac{\rho U^2}{\gamma^* L}$$
1.4

where ρ is the water density, γ^* is the volumetric weight which is a ratio of the netting weight in the water and the volume.

It was shown that for a Froude number above 130, which is a common case, the effect of buoyancy forces on the shape is not significant (Fridman, AL 1973). The Reynolds number was assumed to have a negligible effect on the drag coefficient for model experiments conducted in the subcritical flow regime. Dynamic similarity was proposed by keeping the ratio of static (generated by rigging) and hydrodynamic forces constant, namely Newton's number:

$$Ne = \frac{q}{\rho L^2 U^2}$$
1.5

where q are the static forces generated by rigging.

In trawl modelling, an important condition is to ensure that the netting solidity, the ratio of twine area to projected area, is similar between the model and full-scale. It is often impossible to scale down twine diameter and mesh size proportionally, which results in net blockage area being different between the model and prototype, and hence may lead to scaling miscalculation. Tauti (1934), Dickson (1961) and Fridman (1973) suggested using full-scale material in model experiments. These experiments are commonly conducted in flume tanks and wind tunnels. In a flume tank setup, the flow velocity and consequently hydrodynamic force have to be scaled down to minimize turbulence and wall proximity effects. For prawn trawls, which are built from significantly stiffer materials compared to fish trawls, the use of full-scale

material may be impractical if mechanical forces dominate over hydrodynamic forces, and thus, the obtained data is inaccurate. Flesser (1994) studied the effect of selvage tapers on the engineering performance of the Florida Flyer by testing full-scale trawls in a flume tank. The obtained data seems to be inconsistent, which was explained by 'the wrinkle effect' (Fig. 1.8). The problem occurred due to the hydrodynamic force being too low to overcome net stiffness and to enable the trawl to gain a proper shape.

The relation of hydrodynamic forces and net stiffness has not been largely addressed. Christensen (1975) considered stress-strain characteristics for fishing net modelling, but in respect to net material only. However, hydrodynamic forces are coupled to structural forces, and hence the relation of the former and the latter has to be established for accurate modelling. Tsurkov et al. (2011) experimentally estimated the drag for copper alloy nets. Their comparative analysis with previously published formulae on nylon net drag coefficient led to the conclusion that net flexibility should not be assumed negligible for quantifying the net drag coefficient.
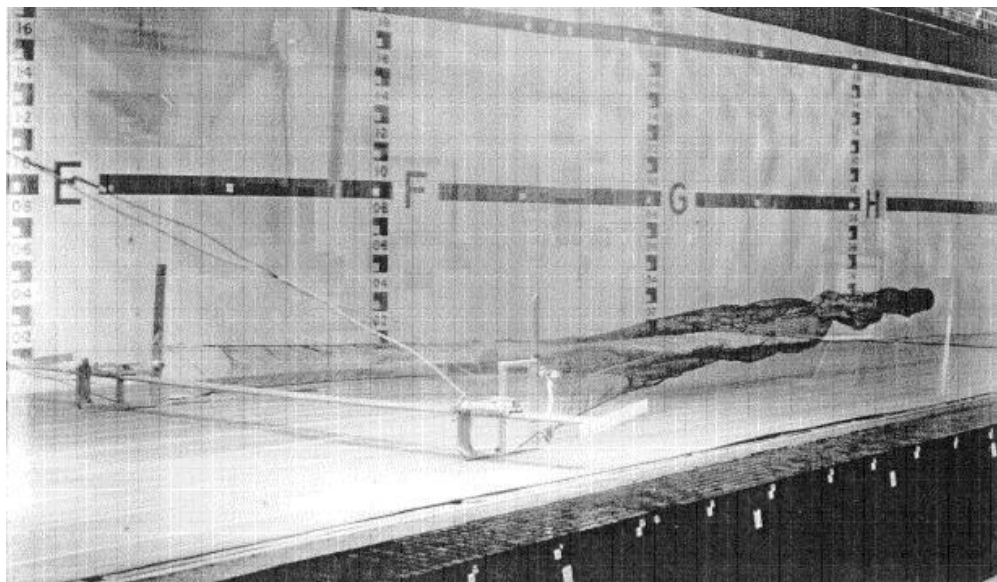
Fig. 1.8 A prawn trawl tested in a flume tank (Flesser 1994).
The net wrinkling, especially in the aft part of the trawl, can be clearly seen.

1.5 Prawn trawl drag variables

As mentioned above, there is a non-linear relationship between trawl shape and hydrodynamic forces. Thus, to study a relation between net stiffness (shape) and hydrodynamic forces, it is initially necessary to consider the specific prawn trawl parameters which impact the drag force. According to hydrodynamic theory (Morison's eq.) (Fredsøe & Sumer 1997), the drag force is proportional to the flow velocity squared and the cross-sectional area, provided the drag coefficient is independent of the Reynolds number. This is valid for solid bodies as their shape remains constant; the orientation of the body is the only other concern. A net is a system with multiple degrees of freedom which undergoes large deformation under external and internal forces. A prawn trawl represents a complex engineering structure, due to the structural compliance of the netting. The net changes its shape under the load, but as the shape changes, the loads are also changing, so there is a strong compliance coupling with hydrodynamic forces.

Angle of incident flow, net porosity and Reynolds number.

Table 1.1 Various reports on parameters that determine the drag coefficient of the plane net at a low angle of attack (Re is Reynolds number, S_d is netting solidity (blockage) and α is an angle of attack).

Study	Parameters considered	Parameters affecting the drag coefficient
Taniguchi (1968)	Re, S_d=const, α =const	Re
Dvernik (1971)	Re, S_d, α	α
Aarnes et al. (1990)	S_d, α	S_d, α
Buxton & DeAlteris (1993)	Re, S_d, α =const	S_d
Gjøsund & Enerhaug (2010)	Re, S_d, α =const	Re, S_d

For the nets exposed to the flow at a low angle of attack, previously-published results show inconsistency in the way the Reynolds number, netting porosity and a low angle of incident flow affect the drag coefficient (a comparison summary is presented in Table 1.1). A definition of an angle of attack α between the net and flow is provided in Fig. 1.9. The Reynolds number Re is based on twine

diameter. Netting solidity S_d is the ratio of twine area and overall area covered by the net. Netting porosity is the ratio of twine-free area and overall area covered by the net. As both parameters, netting solidity and porosity, quantify a relative net blockage area, they are interchangeably used in the literature.
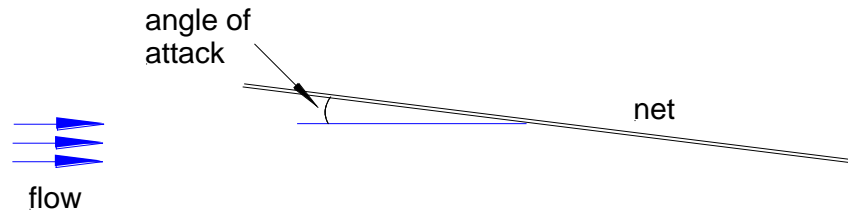
Fig. 1.9 Definition of angle of an attack α between the net and incoming flow.

Dvernik (1971) experimentally investigated the drag force for kapron nets (type of nylon) at low angles of attack between 6^0 and 14^0, and $10^3<Re<10^4$. The drag coefficient was approximated as a linear function of the angle of attack α. However, the experimental results from Taniguchi (1968) showed that the drag of a conical shape net that produced an angle to the incident flow of 12^0 strongly depended on the Reynolds number. Buxton and DeAlteris (1992) empirically investigated the drag coefficient of various porosity nets exposed to the flow at an angle of 8.2^0 in a Reynolds number range between 10^2 and 10^3. According to their data, the drag coefficient weakly depends on the Reynolds number, while net porosity has a pronounced effect on the drag. A similar effect of the Reynolds number on the drag coefficient is shown by Gjøsund & Enerhaug (2010). Aarsnes *et al*. (1990) established empirical formulae for the drag coefficient of plane nets in a steady current as a function of angle of attack and net solidity (a ratio of twine area to the area covered by the net). As the Reynolds number is not incorporated into the formula, it can be applied for the subcritical flow regime only ($10^3<Re<10^5$) in which a change in the Reynolds number does not largely affect the drag coefficient. In model testing and full-scale situations, however, nets are often exposed to the flow that corresponds to the Reynolds number below 10^3. Fridman and Danilov (1967) developed a drag coefficient formula for plane nets perpendicular to the flow incorporating the Reynolds number; and Balash *et* al. (2009) derived a steady drag coefficient for plane nets as a drag coefficient for cylinder modified by a function of net

solidity. Both studies showed that for cases of the Reynolds number being below 10^3, the Reynolds number significantly affects the net drag coefficient, in a trend similar to what occurs for circular cylinders. However, the dependence of the drag coefficient on the Reynolds number for the net at a low angle to the flow remains inconclusive.

Netting material

Lowe (1996) investigated the drag saving potential for Spectra netting compared with polyethylene netting prawn trawls. Spectra permits higher breaking strength, so for similar breaking strength, 49% thinner twine was used to build spectra trawls. Twine reduction visibly resulted in a decrease in the drag force. However, in a non-dimensional form, as can be seen in Fig. 1.10, the drag coefficient for spectra netting is on average 10% higher compared to polyethylene; it varies 3-14% depending on the spread ratio. The drag variability could occur due to different material stiffness. Additionally, Balash et al. (2009) studied the drag force on plane netting samples and a similar tendency was detected. However, since construction properties of netting (twisted or braided) were not considered, it remains inconclusive to what extent netting material affects the drag coefficient. In addition, even though an allowance for knotted netting was incorporated through the net solidity, but knots might also affect the elastic properties of netting.
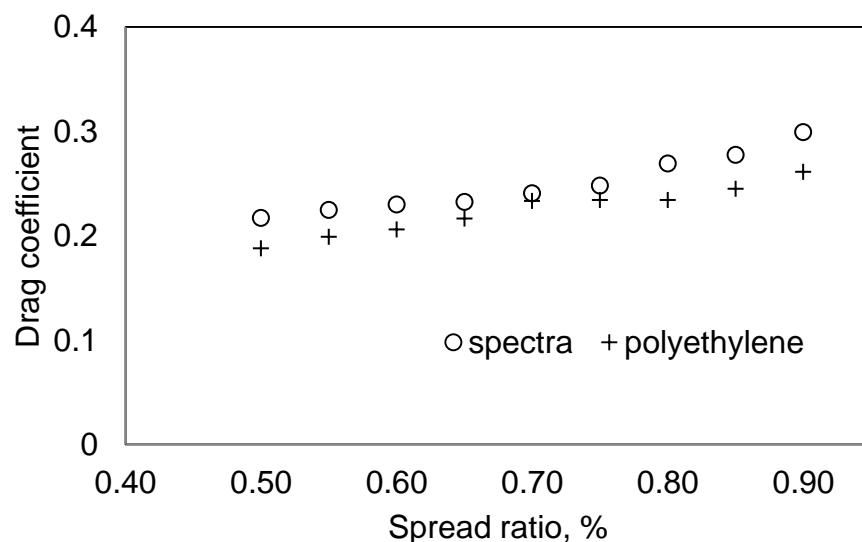
Fig. 1.10 Drag coefficient for prawn trawls of equal design and different netting material (spectra and polyethylene). Sea-trials data for a constant towing speed of 1.6m/s (Lowe 1996).

Horizontal trawl spread

Wakeford (1994) examined the effect of prawn trawl design features on the engineering performance which included, but was not limited to dependence of the drag force on the spread ratio. The spread ratio is defined as the percentage of the net spread to the headline (Fig. 1.11). The study determined optimal spread ratios for prawn trawls of different frame line taper sequences. It also quantified the dependence of the drag coefficient on the spread ratio for the selected trawl designs.
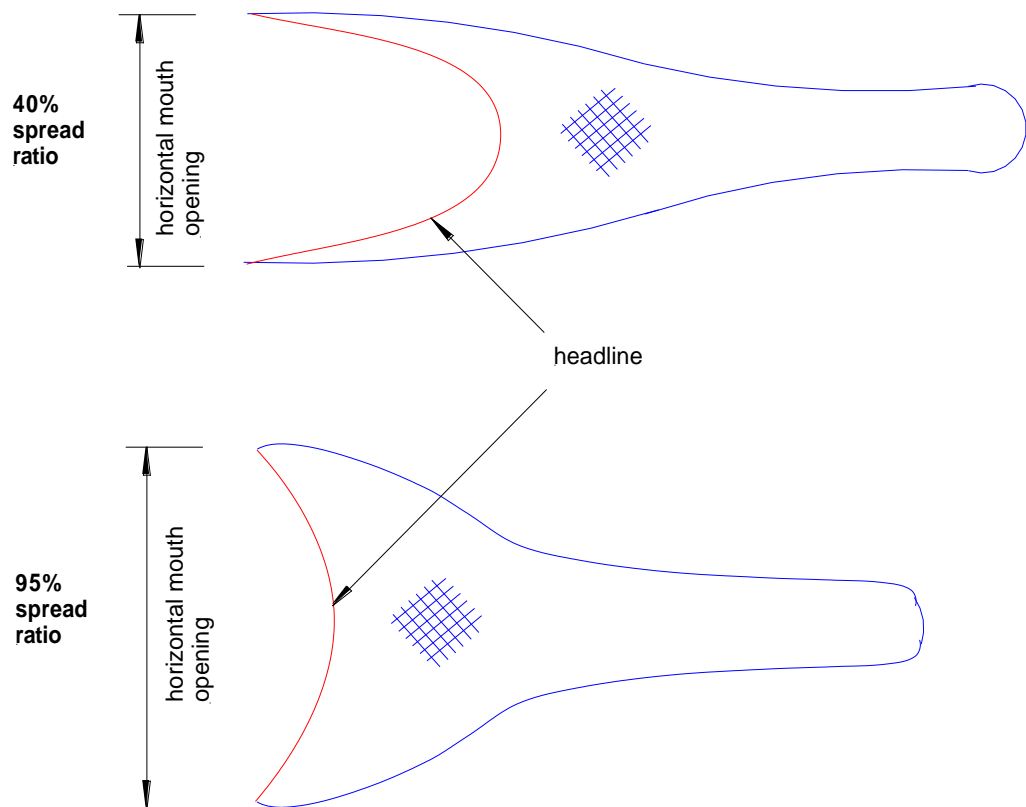
Fig. 1.11 The schematic examples of the netting part with 40% and 95% spread ratio. The spread ratio is defined as the percentage of the headline to the horizontal spread.

Knots

Baranov (1960) reported that knots have a negligibly small effect on the drag coefficient, similar to the effect of the intersecting points in knotless nets. However, Milne (1979) experimentally derived formulae for the drag coefficient of plane nets in a steady current specifically for knotted and knotless netting. As can be seen from Fig. 1.12 and Fig 1.13, the discrepancy in the drag coefficient between knotted and knotless nets linearly increases as net solidity increases (from 3% to 20%). As knot size is primarily a function of twine thickness, it is reasonable to assume that Milne considered the effect of knots on the drag coefficient by accounting extra solidity produced by knots. In experiments with plane nets, samples have to be restrained in a frame. Thus, if knots affect the drag force not only by increasing solidity, but by impacting the net shape, the effect would not be significant enough to be noted in the plane nets experiments. Trawls, however, are only restrained to a certain extent in their forepart by using otter boards to spread their opening. Tait (1987) conducted full-scale experiments at sea to investigate the effect of knots on the drag force of demersal (bottom) trawl nets. An average drag reduction of 12% for knotless trawls was found. However, the twine thickness for knotless and knotted trawls was not exactly equal. There is no evidence in the paper that the allowances were made for this difference. Thus, it remains uncertain to what extent knots contribute to the drag force.

Summary

Summarizing, the following parameters impact the drag force of trawls (in addition to those inherent for solid bodies):

- netting material;
- netting construction properties (braided or twisted);
- the knot factor (knotless or knotted netting);
- net design (sequence of tapers);
- trawl spread ratio.

These parameters are considered in experimental methodologies described in further chapters.
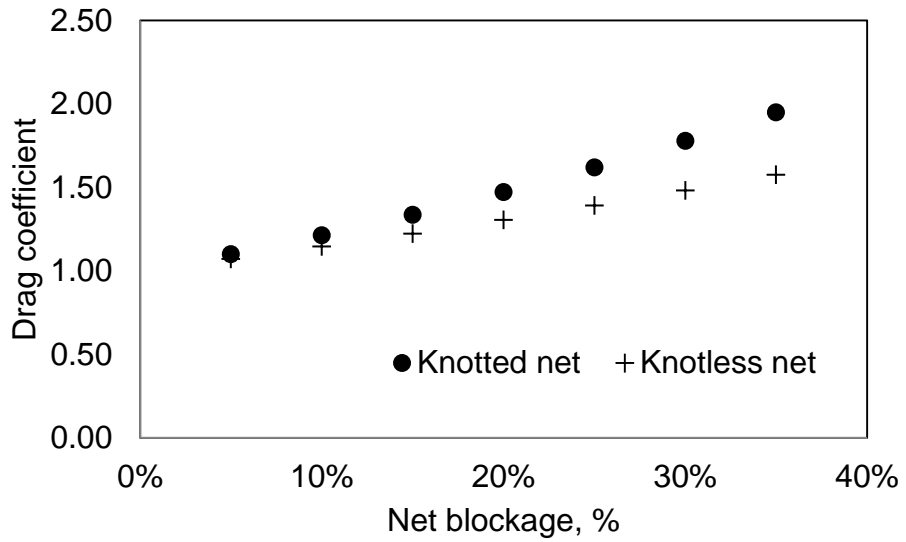
Fig. 1.12 Drag coefficient vs. net solidity for knotted and knotless plane
nets according to empirical formulae by Milne (1979).

$y = 0.5938x + 0.4252$
$R^2 = 0.999$
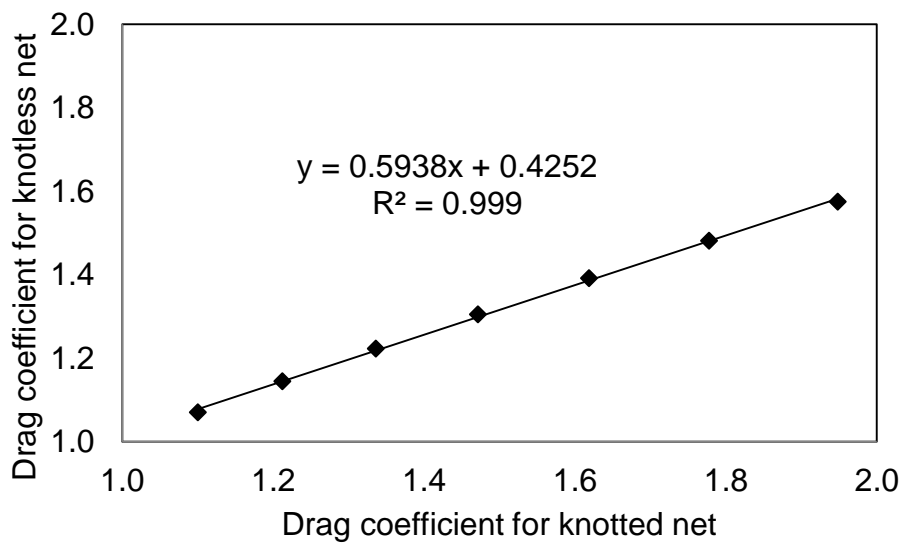
Fig.1.13 Drag coefficient for knotted net vs. knotless net
according to empirical formulae by Milne (1979).

Chapter 2
Net geometry estimation

This chapter reviews existing methodologies for twine geometry measurements. Given results' uncertainty from these methods, a photogrammetric technique was developed in this study, and results for four nets commonly used by the industry are presented. The error in the drag coefficient due to the error in net porosity and twine diameter were also estimated.

2.1 Overview of existing techniques

Fishing gear, and prawn trawls in particular, are mainly constructed out of textile netting. As shown in Fig. 1.2, in prawn trawls, during trawling the netting is responsible for on average 2/3 of the total water resistance from the boat and gear. Hence, accurate net geometry estimation is crucial for drag force prediction. Various techniques have been developed by researchers and fishermen to estimate twine thickness, mesh and knot size.

To measure twine thickness, vernier callipers are commonly used; however, the results are biased due to the operator's variability in compressing of the twine by the callipers. A more accurate yet simple technique was developed in Japan (JCFA 1964). In this technique, a sample is wound around a circular cylinder a number of times, and the measured breadth is divided by the number of the rounds. However, the tightness and the closeness of the rounds are uncontrolled, and hence the accuracy is still variable.

Twine manufacturers commonly provide the *R-tex* number or the Runnage. The *R-tex* is the linear density of the netting yarn or twine in grams per kilometre (Fridman 1986). Alternatively, *R-tex* can be represented through the Runnage (meters per kilogram). The diameter then can be estimated from eq. 2.1:

$$d = K_{DT} (\frac{Rtex}{1000K_t})^{0.5}$$
2.1

where *d* is the twine diameter, K_{DT} and K_t are empirical coefficients (the coefficients are dependent on the netting material). For a given material, they vary by about 30% due to variation in construction properties, and thus the actual and calculated diameters may significantly differ.

Special gauges of various configurations have also been designed. Such gauges can be used for netting made from firm and braided twines only (Fig. 2.1) as the method does not allow estimating effective diameters of twisted twines (Fig. 2.2).

Fig. 2.1 A sample of braided twine.

Fig. 2.2 A sample of twisted twine.

Mesh size is conventionally defined as the distance between two opposite knots or intersecting points. O'Neill (2003) examined the theoretical effect of twine bending stiffness, frictional resistance, boundary slope, gauge force and gauge thickness on mesh measurement. However, the study considered idealised netting, which implied a great number of assumptions, and thus the results are

approximate. Fonteyne et al. (2007) performed a comprehensive review of the existing methodologies and their shortcomings.
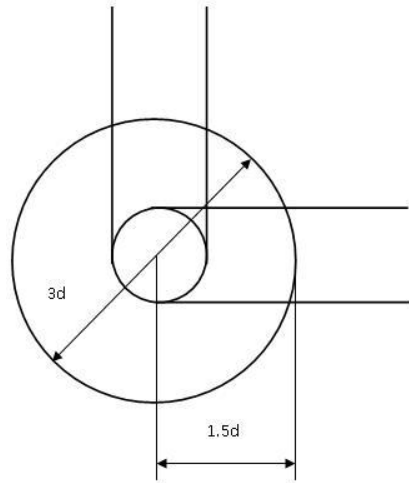
Fig. 2.3 The approximation of the knot size and shape by Fridman (1973).
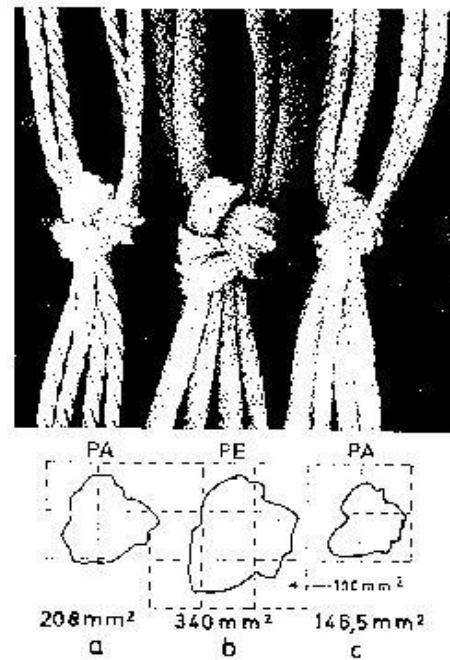
Fig. 2.4 The areas covered by the knots (Klust 1982), Fig. 33).

Fridman (1973) approximated the knot as twine over which other twine is wound (Fig. 2.3). Klust (1982) estimated the knot sizes by applying a photographic method. As can be seen from Fig. 2.4, the knot size may depend greatly on the construction properties of netting. The samples *a* and *c* are made of the same material (polyamide), but one is twisted and another is braided. Both samples are of similar twine thickness, but knot sizes differ greatly.

2.2 The photogrammetric technique for netting porosity estimation

As discussed in the previous sections, the techniques for twine thickness, knot and mesh size estimation do not provide definite results. In an attempt to have an accurate tool for net geometry estimation, a digital photogrammetric technique was developed. A photographic image of a sample was taken and processed with a code developed in this work in the Matlab environment.

Conceptually, the code compares the number of pixels associated with the object (netting) to the number of remaining pixels (background).

There has been a significant amount of research conducted to develop techniques for distinguishing an object from the background. Pixels have to be classified as dark and light to distinguish dark objects from a light background (or vice versa). It is necessary to determine an optimal pixel classification (threshold) so a pixel belongs to the correct group (object or background). Extensive surveys of those techniques were performed by Weszka & Rozenfeld (1978). Otsu (1979) suggested a simplistic method of the threshold corresponding to the minimum sum of weighted-group variances. This is equivalent to selecting a threshold that minimizes the squared difference between the group means. This approach provides an optimal and automatically-selected threshold. It was implemented here in Matlab with the $graythresh$ function. The example of this function application is presented in Fig. 2.5.
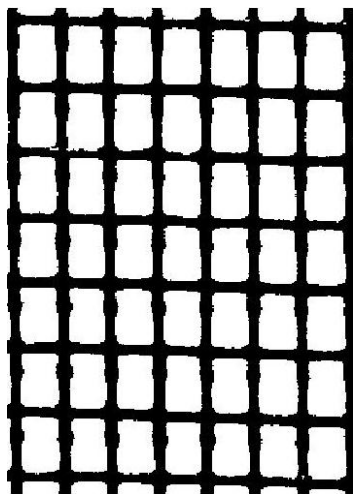
Fig. 2.5 The Otsu's (1979) method threshold application in Matlab for a mosquito screen (image is enlarged).
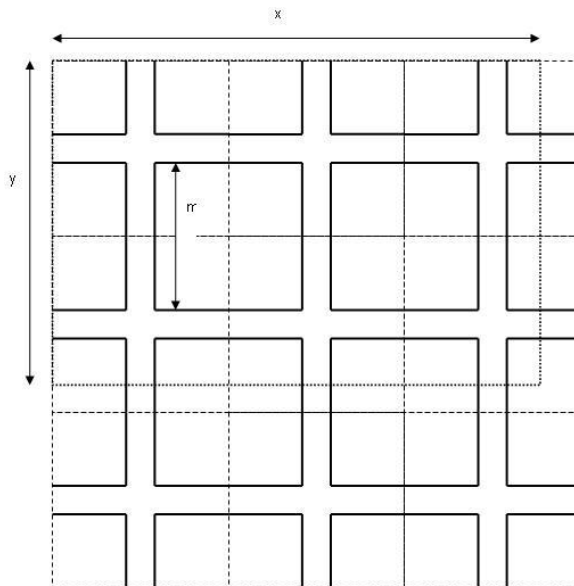
Fig. 2.6 Idealized mesh grid.

Once the pixels were distinguished between the sample and the background, the porous, twine and the total areas were calculated. The porous area was

calculated by applying the `bwarea` function which estimates the number of *on* pixels in a binary image.

The total area was calculated by the multiplication of the image dimensions:

```
[x,y] = size(img)% image dimensions
Aout = x*y% projected area (total image area)
```

The twine area was found from the difference between the total and the porous area:

```
A = Aout-Pr% twine area
```

As can be seen from Fig. 2.6, the mesh bar *m* can be found as follows:

$$\frac{A_{porous}}{P} = \frac{m^2 n}{4mn} = \frac{m}{4} \qquad\qquad 2.2$$

where A_{porous} is porous area, *P* is outside mesh perimeter and *n* is a number of meshes. To estimate the perimeter, the *bwperim* function was used, which ultimately detects the edges of the object (Fig. 2.7) and counts a pixel as a part of the perimeter if it is non-zero (black) and connected to at least one zero-valued pixel (white).

Fig. 2.8 Idealized mesh sketch.

Fig. 2.7 The outside perimeter (edge detecting) of a mosquito screen.

The netting solidity is a ratio of netting area *A* to total (outline) area A_{out}:

$$S_d = \frac{A}{A_{out}} = \frac{2md + d^2}{(m+d)^2}$$

2.3

where d is twine diameter as shown in Fig. 2.8. Thus, twine diameter d was found from solving the quadratic eq. 2.3.

2.3 Error analysis

The following factors introduced error:

- Image resolution
- The number of meshes per image
- Lighting
- Calibration errors

Image resolution

Net solidity is the ratio of the projected netting material to the total outline area of a sample (eq. 2.3). If mesh size and twine diameter are measured in pixels, then the number of meshes per image can be estimated as follows:

$$n_1 = \frac{xy}{(l+d)^2}$$

2.4

where x and y are image dimensions in pixels (Fig. 2.6).

The number of meshes calculated from eq. 2.4 is most likely not an integer. The accurate solidity is estimated with number n_1 rounded to the integer n. The difference between n and n_1 represents the solidity error due to the possible incorrect ratio of twine to porous pixels. Thus, the error can be estimated as follows:

$$\varepsilon[S_d] = \frac{n_1 - n}{n} * 100\%$$

2.5

26

As seen from eqs. 2.4 and 2.5, the error clearly depends on mesh geometry (twine diameter and mesh size) and image dimensions. Provided the image dimensions are constant, the error is solely a function of twine diameter and mesh size. The actual minimum number of meshes required to have a negligible error (i.e. less than 0.1%) varies from sample to sample. On average about 100 meshes per image produces less than 0.1% error for the samples tested (Fig. 2.9). The logarithmic graph of Fig. 2.9 (shown in Fig. 2.10) also illustrates that the model is 1-st order convergent or better.

In general, for low solidity (highly porous) nets, the error is greater as a smaller number of meshes is included in the image. However, even for low solidity nets numbers n and n_1 may equal each other in case when xy equals $(l+d)^2$ in eq. 2.4, and hence the error in solidity would be zero. Due to this arbitrary variation between image dimensions and netting solidity, some points on Fig. 2.9 do not fit the trend line.
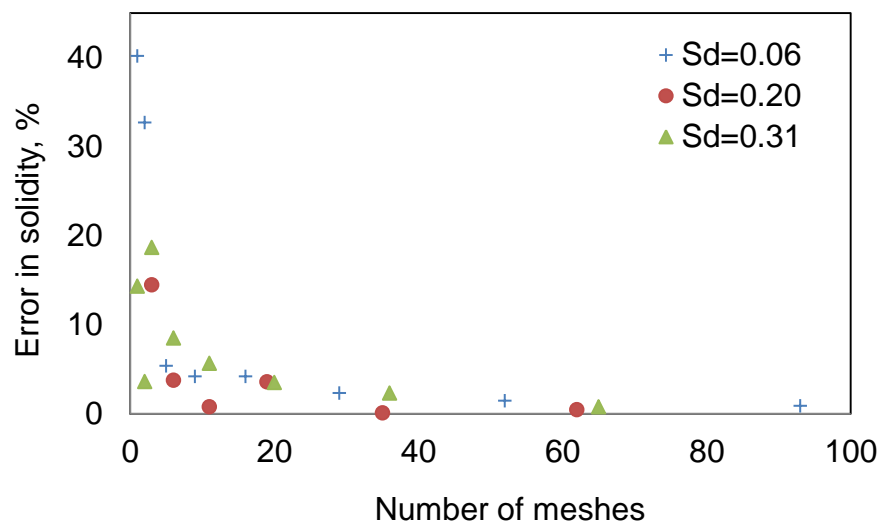
Fig. 2.9 The effect of mesh number per image on solidity error for three types of solidity (low, average and high).
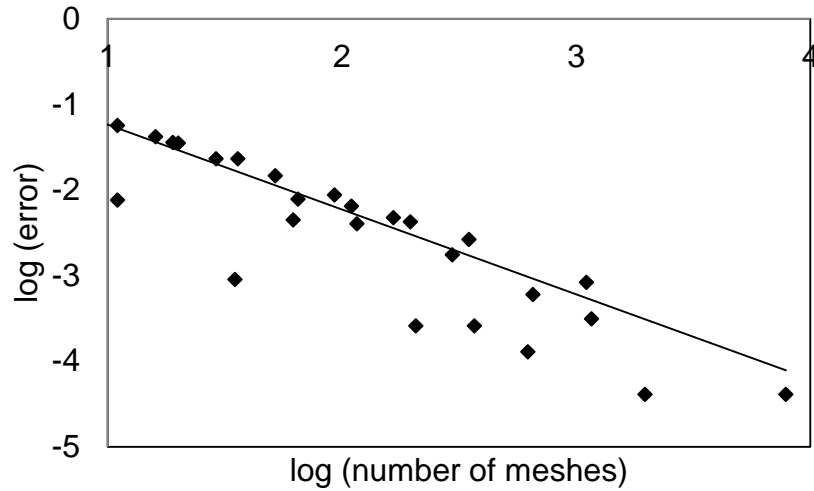
Fig. 2.10 The logarithmic representation of Fig. 2.9.

Lighting

Lighting may produce shadow or blurred lines. To minimize the error, constant lighting conditions (amount of light and angle between the light source and the object) were maintained.

Twine thickness

If the actual twine thickness is 1mm and is calculated to be 50 pixels, the potential error is of maximum 1% (in the case of the actual thickness being 49.5 pixels, due to pixilation error, an incorrect value of 50 will be recorded). It is not always practically possible to simultaneously satisfy the conditions of the minimum number of meshes and minimum image resolution. However, as demonstrated in the following section, an error of even 5% for twine thickness produces an error of around 1% in the drag coefficient for high solidity nets.

The error in the drag coefficient due to the error in solidity and twine diameter

Balash et al. (2009) developed an empirically based formula to estimate the drag coefficient of plane nets exposed perpendicularly to the flow:

$$C_{D[net]}^{out} = C_{D[cyl]}[8.03S_d^2 - 0.74S_d + 0.12] \qquad 2.5$$

where $C_{D[net]}^{out}$ is the drag coefficient for the net as a function of the outline area, $C_{D[cyl]}$ is the drag coefficient for the circular cylinder, and S_d is the net solidity. Applying Taylor's expansion of a differential series, the error in the drag coefficient can be estimated as follows:

$$\varepsilon[C_{D[net]}^{out}] = \left[\left(\varepsilon_{S_d} \frac{\partial C_{D[net]}^{out}}{\partial S_d}\right)^2 + \left(\varepsilon_d \frac{\partial C_{D[net]}^{out}}{\partial d}\right)^2\right]^{0.5} \qquad 2.6$$

where $\varepsilon[C_{D[net]}^{out}]$ is the error on the drag coefficient; ε_{S_d} is the error on net solidity; ε_d is the error on twine diameter. According to White (1974), drag coefficients for circular cylinders can be reliably estimated for a Reynolds number below 5×10^3, which is a typical flow regime for nets, as:

$$C_{D[cyl]} \approx 1 + \frac{10}{Re^{2/3}} \qquad 2.7$$

Thus, the definite error on the drag coefficient can be found from the following equation:

$$\varepsilon[C_{D[net]}^{out}] = [((\varepsilon_{S_d} C_{D[cyl]}(16.06S_d - 1.48))^2 - (\varepsilon_d \frac{20}{3} Re_{[cyl]}^{-2/3} \frac{1}{d}[8.03S_d^2 - 0.74S_d + 0.12])^2]^{0.5} \qquad 2.8$$

An error of 0.1% in solidity coupled with an error of 1% in twine diameter generates on error of around 0.6 % in the drag coefficient for high solidity netting, and if the error on twine thickness is 5%, the drag coefficient error is around 1.2% (Fig. 2.11). However, this is valid for nets placed perpendicular to the flow direction.

Twine thickness was estimated for a number of braided samples by applying the image analysis method, and the results were compared with manual

measurements obtained by vernier callipers (Fig. 2.12). As can be seen, with the exception of one sample, there is a steady off-set of about 5% between the two methods. This difference has been attributed to the compression of the twine by the vernier callipers.
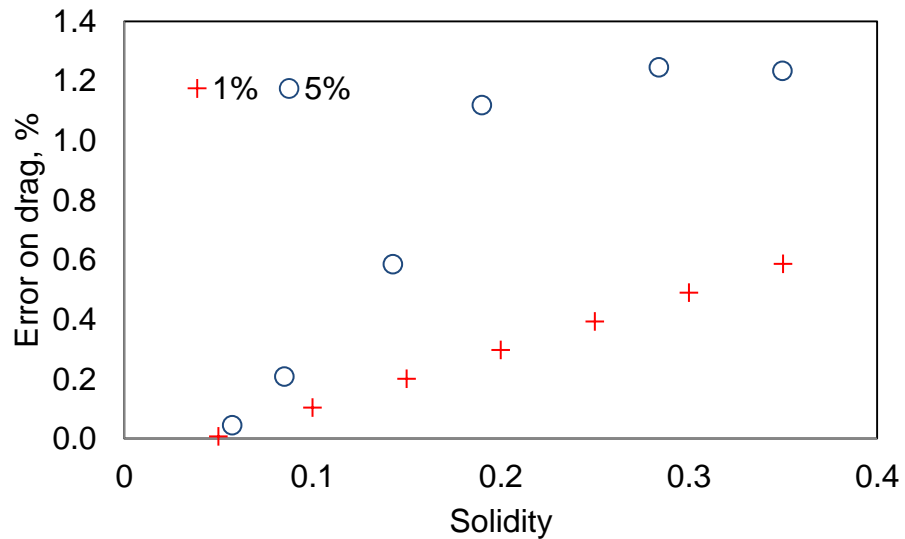
Fig. 2.11 The error in the drag coefficient for plane nets produced by an error of 0.1% on net solidity and an error of 1% and 5% in twine thickness.
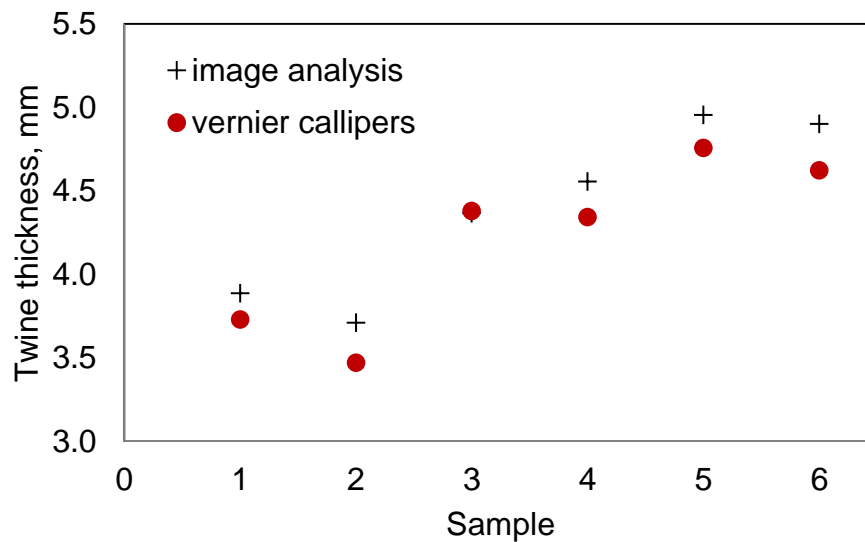
Fig. 2.12 Twine thickness obtained by measurements with vernier callipers and image analysis.
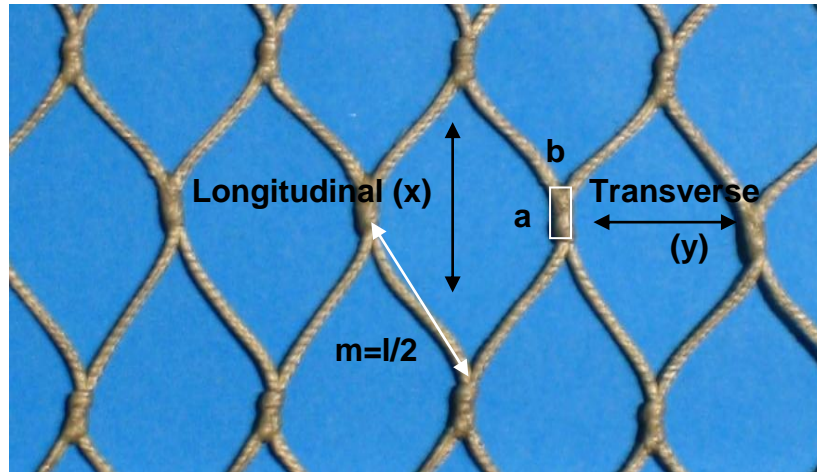
Fig. 2.13 Mesh orientation specification.

2.4 Results

Four prawn nets that are commonly used by the trawl operators in Australia were chosen. The list of the samples and net geometry results are shown in Table 2.1. By choosing these four samples, this study considered including knotless, single and double knotted nets. Mesh and knot sizes were estimated with vernier callipers. Twine thickness and solidity was estimated by applying the photogrammetric technique – this accounted for irregularity of knot shape. As, knots restrained mesh opening in a transverse direction, mesh size was measured in longitudinal and transverse directions.

Table 2.1 Net geometry (mesh geometry is specified in Fig. 2.13)

	Retail name	Construction properties	Effective twine diameter	Mesh size (longitudinal x transverse)	Knot size	Solidity
			d	$l=2m$	$a \times b$	S_d
			mm	mm	mm	-
1	24ply Polyethylene	400 denier twisted 24 ply single knot	1.68	52.1 x 49.71	5.24 x 4.32	0.150
2	Ultracross Dyneema	1.1mm braided knotless	1.28	51 x 51	1.9 x 1.9	0.980
3	Hampidjan Dynex	1.0mm braided double knotted	1.26	50.25 x 42.05	6.8 x 3.3	0.108
4	Euroline Premium Plus	1.0mm braided single knot	1.40	52.06 x 49.51	5.12 x 4.12	0.121

Chapter 3
Flexural rigidity estimation

This chapter describes a new method for quantifying the stiffness or flexural rigidity of netting. Flexural rigidity figures for four prawn nets were obtained by employing the method and existing analytical approximation techniques. The flexural rigidity results are used in the next chapter to allow the variation in prawn trawl drag with respect to flexural rigidity to be defined.

3.1 Overview of existing techniques

Brandt & Carrothers (1964) referred to flexural rigidity EI as the force required to cause a unit of bending deflection. Flexural rigidity EI is a product of modulus of elasticity E (GPa or kN/mm^2) and second moment of inertia I (mm^4).

When stiff material is used to build fishing gear, flexural rigidity restrains twine bending and mesh opening (Lowry & Robertson 1996), which result in (1) a greater twine area exposure to the flow causing a drag increase, and (2) also minimises chances of small non-targeted species to escape the trawl. Though net stiffness for certain types of fishery can have significant drag and selectivity implications, little research has been undertaken to quantify net flexural rigidity and establish its effect on trawling performance.

O'Neill (1997) and (2002) analytically derived a solution to estimate mesh deflection as a function of flexural rigidity, mesh size and tensile forces (eqs. 3.1

and 3.2). He found an asymptotic solution for differential equations that governs twine bending stiffness. The proposed solution assumed that twine bending moment is proportional to its curvature. Although real twine often bends non-linearly, O'Neill's analytical approximation (eq. 3.1 and eq. 3.2) is accurate for $(EI \cdot f / m^2) < 0.04$, where f is applied tension, and m is a length of mesh bar. Sala et. al. (2007) designed an apparatus to measure mesh opening variation under loads for small netting panels of 3 x 3 meshes. Then, a regression analysis was applied to calibrate O'Neill's analytical model to fit the experimental data:

$$x = a + m\cos\beta + 4\sqrt{\frac{EI}{f}}[\cos(\frac{\theta+\beta}{2}) - \cos\beta] \qquad 3.1$$

$$y = a + m\sin\beta + 4\sqrt{\frac{EI}{f}}[\sin(\frac{\theta+\beta}{2}) - \sin\beta] \qquad 3.2$$

where x and y are mesh opening in longitudinal and transverse directions respectively, a and b are knot dimensions as specified in Fig. 2.13, f is tension estimated as a vector summation of the respective tensile components: $f = (f_x^2 + f_y^2)^{0.5}$, θ is slope angle, and $\beta = tan^{-1}(f_y/f_x)$.

As can be seen from Fig. 2.13, variable x and y are interdependent: if the mesh opening is increased in the longitudinal direction, it is decreased by the equal amount in the transverse direction. The regression model developed by Sala et al. (2007) showed inconsistency between the results for x and y. The authors reasoned the discrepancies by the fact that only the x component of the tension f was measured in the experiment. Prior & Cognard (2011) established a method to quantify net flexural rigidity and compared their results with Sala et. al (2007) - the figures between two studies vary significantly (up to an order of magnitude).

The present study aimed to investigate resistance of mesh opening in prawn nets, and to develop a tool for estimating the flexural rigidity of netting. The knowledge of mesh opening resistance will advance the optimisation of fishing

gear in terms of selectivity, catching performance, and energy efficiency. In the scope of the present study, results for flexural rigidity were necessary to quantify a relationship between prawn net stiffness and prawn trawl hydrodynamic drag.

3.2 Measurement technique background

In fishing gear design, the concentration of meshes per unit of distance is defined by hanging coefficients. If meshes are evenly hung along the transverse and longitudinal lines, the horizontal and vertical hanging coefficients for a vertical sheet of netting, u_x and u_y respectively, can be found as follows:

$$u_x = \frac{x}{m} = \sin\varphi$$

3.3

$$u_y = \frac{y}{m} = \cos\varphi$$

3.4

where x, y, b and α are geometric mesh parameters as specified in Fig. 3.1
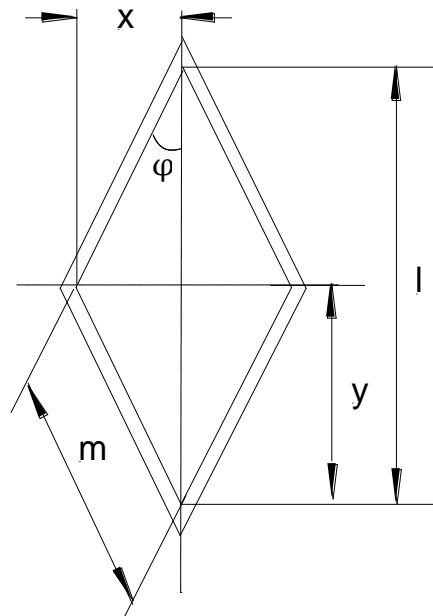
Fig. 3.1 Mesh geometry specification.
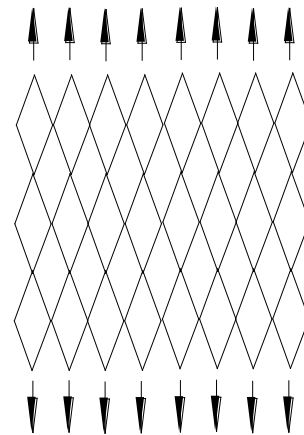
Fig. 3.2 Plane net under the uniform load considered by Baranov (1960).

Baranov (1960) considered the shape of a plane net under uniformly distributed vertical loads (Fig. 3.2). The properties of the net were perceived through the properties of the individual mesh. It was shown that tensions in individual twines depend on the hanging coefficients. The relation of the horizontal tension σ_x and the vertical tension σ_y appeared as follows:

$$\frac{f_y}{f_x} = \left(\frac{u_x}{u_y}\right)^2 = \frac{1}{\tan^2 \varphi} \qquad\qquad 3.5$$

Fridman (1973) stated that if the bottom and top meshes of the net are attached to rings, the net narrows towards the middle due to tensile forces (Fig. 3.3). Hence, based on Baranav's considerations, it can be assumed that the shape of the net restrained between the hoops depends solely on the hanging coefficients, hoop diameter and a number of meshes between the hoops.
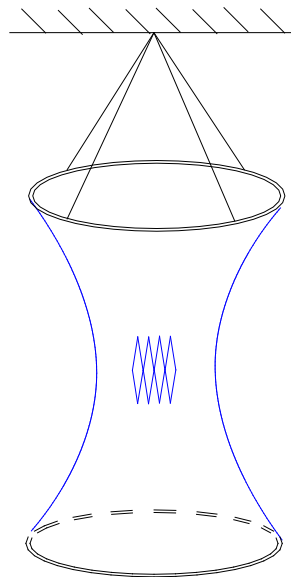
Fig. 3.3 A net sample attached to two hoops.

Andreyev (1960) derived a series of elliptical integral equations that govern the hourglass shape of a net between two hoops (Fig. 3.3). He determined the distance between the hoops as a function of the hoop diameter and hanging coefficients in the middle section. However, as the middle section hanging coefficient is often unknown, the solution is of limited practical applications.

35

3.3 Test objective

The current study measured mesh opening in the middle section of hoop units for netting attached in both longitudinal (standard) and transverse (T90) directions. When the longitudinal net orientation was aligned with the vertical axis, the middle section hanging coefficient and distance between the hoops were not affected significantly by a vertically applied load. The extent of variation depended on the material's elongation properties (tension stiffness) only. When the net was attached to the hoops in T90 configuration such that the low transverse mesh opening was aligned with the vertical axis, the net tended to acquire a cylindrical shape and not an hourglass shape when no load or small load was applied (Fig. 3.4a). As the load increased, the low vertical mesh opening shifted towards the extended opening of the standard case where the mesh-stretch direction was aligned with the axis of the hoop units (Fig. 3.4b, c). The objective of the experiment was to measure vertical mesh opening in conjunction with a load change for the T90 case until it reaches the vertical opening of the standard case.
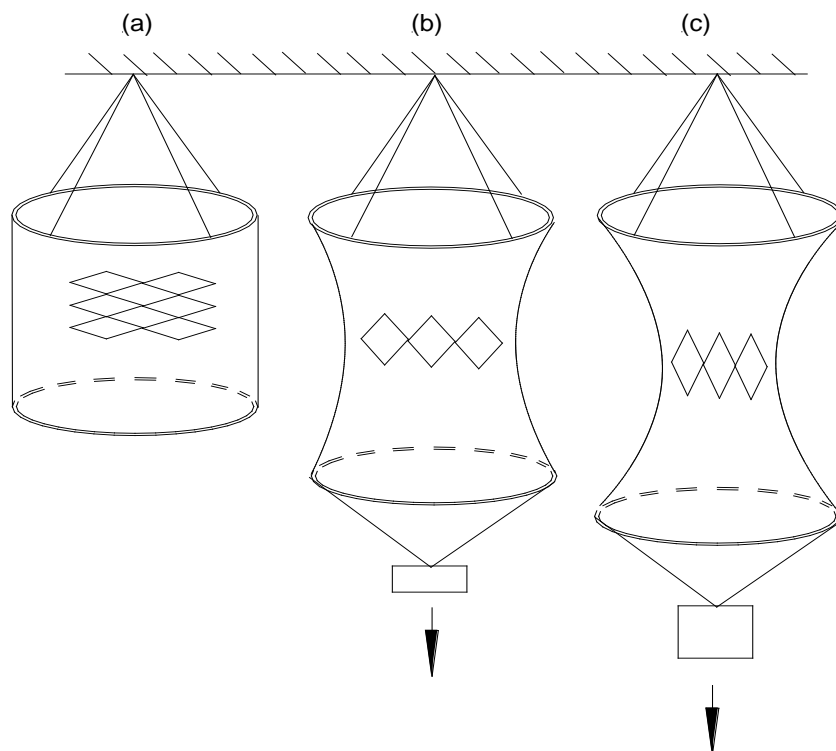
Fig. 3.4 A net attached to the hoops in transverse mesh orientation:
(a) with no load applied (the weight of the net and the bottom hoop only);
(b, c) the net acquires an hour-glass shape as the load gradually increases.

3.4 Experimental set up

A net sheet with an equal number of meshes (39 x 39) in the longitudinal and transverse directions was restrained between two aluminium hoops. The entire system was of an hourglass shape – the top hoop was hung from a single point, and a platform was attached to the bottom hoop for applying weights (Fig. 3.3). The hoop was of 385 mm outside diameter, 22 mm thickness and 700 g weight. Prior to the attachment, the vertical sides of the net sheet were stitched together with a 24ply PE (polyethylene) twine so the sample acquired an enclosed shape. The net was attached to the hoop by twine lacing trough a mesh and around the hoop (Fig 3.5).
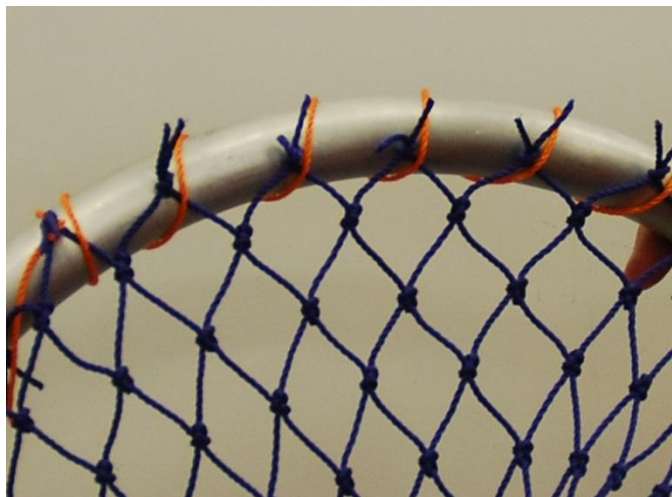
Fig. 3.5 The net laced to the hoop.

When the net was attached to the hoops in the longitudinal orientation, a load of 10kg was applied for the net to overcome mechanical forces and to acquire a firm and symmetrical shape. Three threads were connected to the top hoop equally-spaced along the hoop circumference, and lowered vertically with sinking weights (Fig 3.6). As three measurements of k (the distance between the middle section and the thread (Fig. 3.6b) were taken, it ensured that the system was symmetric in respect to the vertical axis. The results for the measured distance k allowed circumference c_0 and hanging coefficient u_0 calculations for the middle section:

$$c_0 = 2\pi(r - k)$$ 3.6

$$u_0 = u_x c_0 / c$$ 3.7

where r is outside hoop radius, k is the location length as specified in Fig. 3.6, u_x is a horizontal hanging coefficient of meshes on a hoop, and c is a hoop circumference.

The distance between the hoops was also recorded. As mentioned above, meshes do not open transversely as wide as longitudinally due to knots being aligned in the longitudinal direction. Thus to compare the distance between the hoops in the longitudinal and transverse directions, a correction factor was applied − the factor was equated to the ratio of transverse and longitudinal mesh size (Table 2.1).
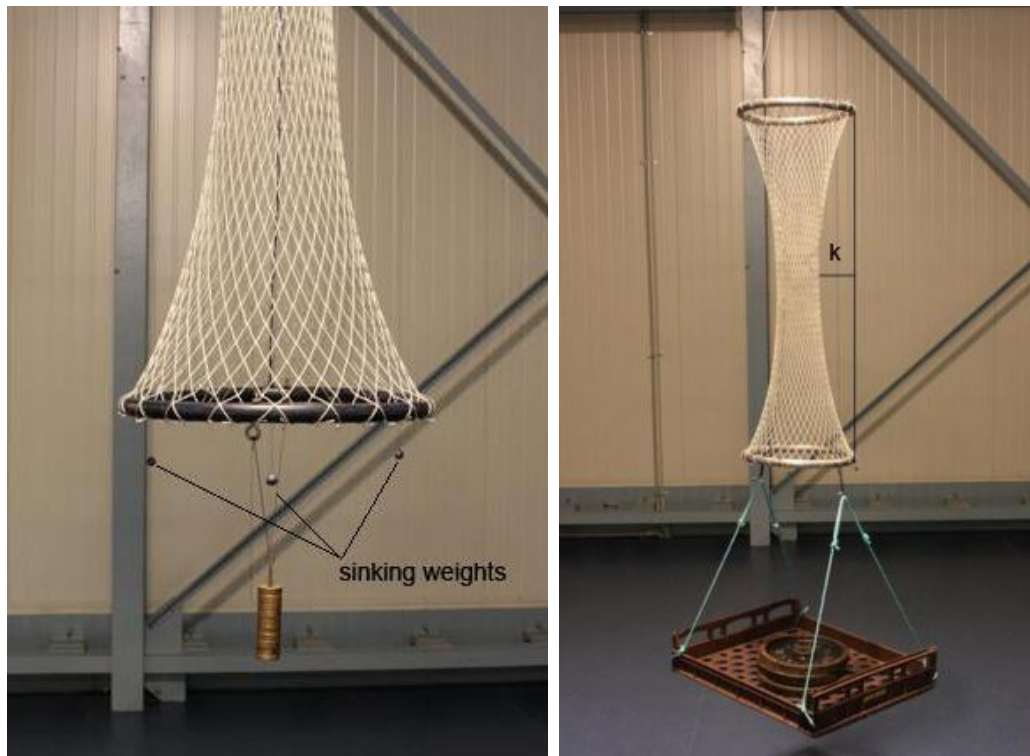
Fig. 3.6 A net restrained between the hoops - experimental set-up: (a) a light polyethylene pipe hoop on the left, (b) and aluminium hoops on the right).

The sample from Dyneema® material (Table 2.1) was very soft, and the weight of the 700g aluminium hoop was expected to result in no difference between the

transverse and longitudinal orientation. To overcome this, two light-weight hoops of 100 g each were made from polyethylene pipe to test the Dyneema® sample (Fig. 3.6a).

As the mesh size slightly varied between the samples (and hence hanging coefficients also varied), it was important to check the extent to which the hanging coefficient for meshes attached to the hoops affected the distance between the hoops. For this, another set of experiments were done with nylon samples (50mm mesh size, single-knotted and twisted twine of 1466Rtex, eq. 2.1 defines Rtex). For every sample, a number of meshes between the hoops were constant, but the number of meshes attached on to the hoops varied. The horizontal hanging coefficient was calculated as shown in eq. 3.8:

$$u_x = \frac{c}{nl}$$

<div align="right">3.8</div>

where c is a hoop circumference, n is a number of meshes attached to the hoop, and l is mesh size. The number of meshes on the hoop n and the resulting hanging coefficients u_x are presented in Table 3.1.

Table 3.1. A number of meshes attached to the hoop and corresponding hanging coefficient (eq. 3.8) for four nylon samples.

number of meshes on hoop n	183	159	147	135
hanging coefficient u_x	0.32	0.37	0.40	0.44

Each sample was restrained between 1m outside-diameter aluminium hoops and the load of approximately 7 kg (including the weight of the bottom hoop and the tray) was applied vertically as shown in Fig. 3.7 so twine-spring memory could be overcome and the net-hoop system would acquire a perfect symmetric shape in respect to the vertical axis. The distance between the hoops was then measured to quantify an extent by which the horizontal hanging coefficient on the hoop affects the distance between the hoops.

Fig. 3.7 Nylon samples in the longitudinal orientation attached to 1m diameter hoops with the horizontal mesh hanging coefficient of 0.32 and 0.44 (eq. 3.8 and Table 3.1). As seen, the distance between the hoops does not significantly change with hanging coefficient variation.

As mentioned above, Andreyev (1960) developed a series of elliptical equations that estimate the shape of the net restrained between the hoops in the longitudinal orientation. As a part of the present study, a Matlab code was developed to solve the equations to compare analytical and experimental results for the longitudinal orientation. The code is presented in Appendix I.

3.5 Experimental results and discussion

Hanging coefficient effect on the distance between the hoops

A change in the distance between the hoops in respect to the hanging coefficient u_x for nylon netting is presented in Table 3.2. The distance k linearly changed with respect to the hanging coefficient u_x – as the hanging coefficient increased (which implied less meshes on the hoop), the system tended to acquire an hour-glass shape (Fig. 3.7), and hence the distance k also increased. A relative variation based on the mean distance between the hoops was less than 2%. This was a case for a wide range of hanging coefficients between 0.32 and 0.44 (35% difference). For prawn net samples examined in the present study (Table 2.1), it

was only a 3.6% difference between the highest and lowest hanging coefficients (due to slight variation in mesh size). Thus, as a high increase of 35% in the hanging coefficient caused only 2% variation in the distance between the hoops, a 3.6% change in the hanging coefficient was assumed to be negligible.

Table 3.2 Measurements for nylon samples.

hanging coefficient u_x	0.32	0.37	0.40	0.44
distance k, mm (Fig 4.6)	67	90	104	127
distance between hoops L_{hoop}, m	2.39	2.38	2.37	2.36

Experimental results vs. analytical prediction

The distance between the hoops for the longitudinal orientation for the nylon samples (Table 3.2) was compared with the analytical prediction by Andreyev (1960). The difference in results was about 1%. However, the theory proposed by Andreyev (1960) can only predict the distance between the hoops based on the circumference of the middle section c_0 (eq. 3.6) which is often unknown. Prior (2001) numerically estimated the shape of a net that was restrained between the hoops (Fig. 3.8). However, as there was no prior knowledge for the netting flexural rigidity figures, the proposed model did not accurately estimate the shape.

Mesh resistance for bending

As expected, when the net sample was attached to the hoops in the transverse orientation, the system initially had a shape similar to that of a circular cylinder, and as the load gradually increased, the system acquired an hour-glass shape (Fig. 3.9). When the net was in the longitudinal orientation on the hoops, a load increase did not affect the shape of the system – the distance between the hoops and middle section circumference remained constant. The Dyneema® sample due to its multi-filament structure was very soft, and the difference between the longitudinal and transverse net orientation was not measurable even using very light polyethylene pipe hoops. Fig. 3.10 illustrates the difference in mesh opening for the longitudinal and transverse orientation for three samples: Hampidjan, 24ply PE and Euroline premium Plus. A mesh opening coefficient

on *y*-axis of Fig. 3.10 is the ratio of middle section mesh opening (eq. 3.6 and 3.7) in the longitudinal orientation to mesh opening in the transverse orientation.
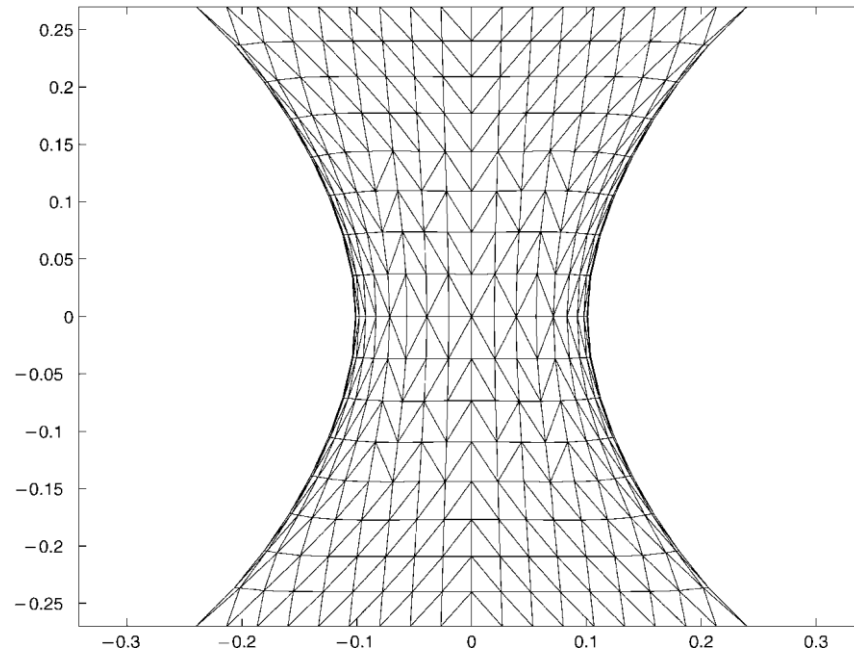
Fig. 3.8 An example of calculated net shape using numerical method of Prior (2001).
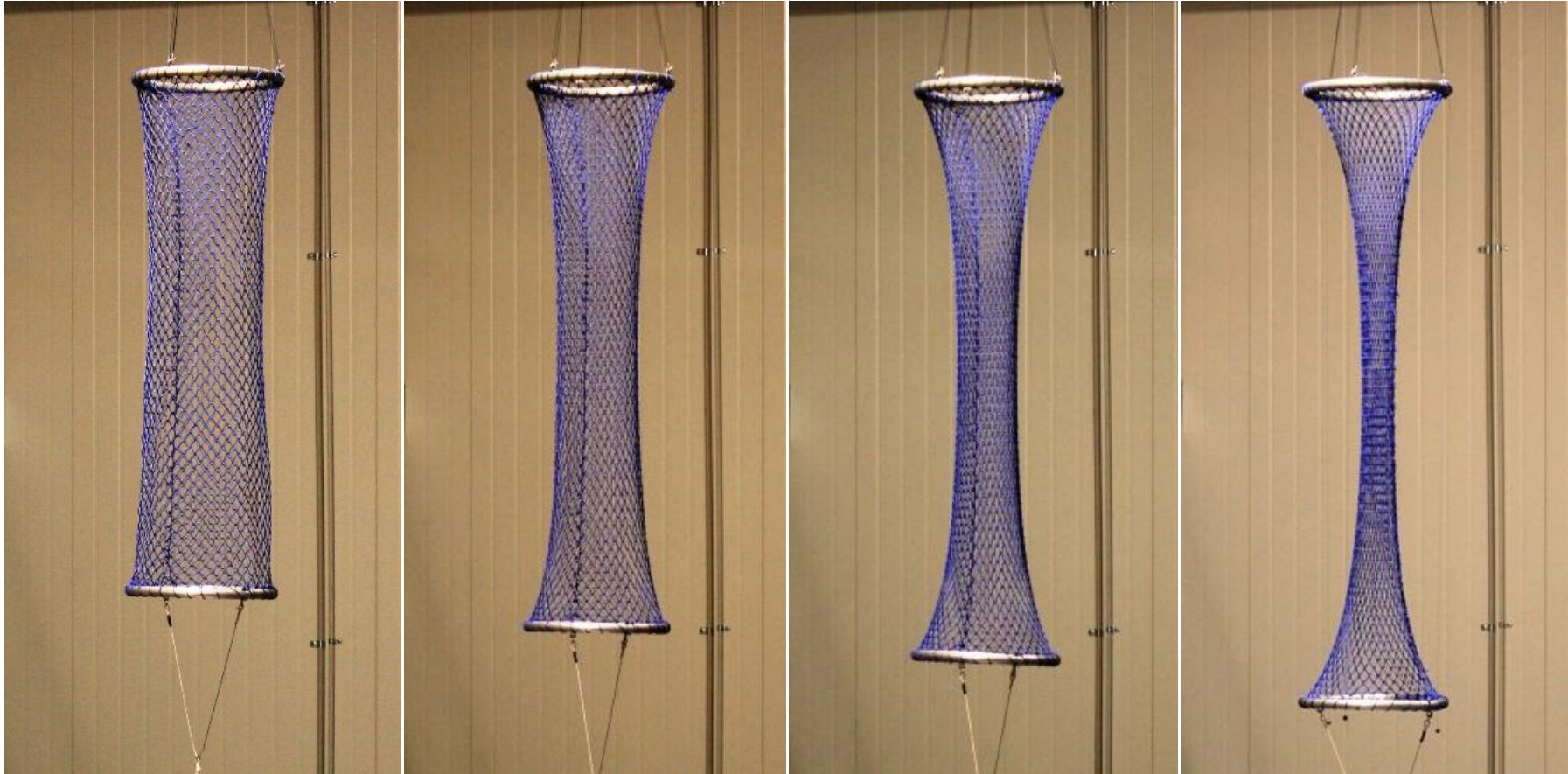
Fig. 3.9 Transversely-oriented net sample under various loads.
As the load increases, the shape of the system gradually acquires an hour-glass.

As seen from Fig. 3.10 initial loads bent the twine more effectively - an increment of 0.5 kg caused a significant change in mesh opening for the loads of up to 3kg, while an effect of load increase over 3kg on the mesh opening was less pronounced. The mesh opening coefficient on *y*-axis of Fig. 3.10 does not reach a figure of 1, which would imply mesh opening in the transverse and longitudinal orientation was equal. The mesh opening for the two orientations could not be equal because the mesh opening in the transverse orientation was restricted by knots being aligned in the longitudinal orientation. If a significantly higher load than in these experiments were applied, it would only cause net damage. The trend lines shown in Fig. 3.10 suggest that the power exponent of the curves approximates to the figure of 0.05. A linear regression analysis was applied to standardise the exponent between the curves. The coefficients *a* of the power functions y=$ax^{0.05}$ from Fig. 3.10 can be then used for relative stiffness comparison between the samples.
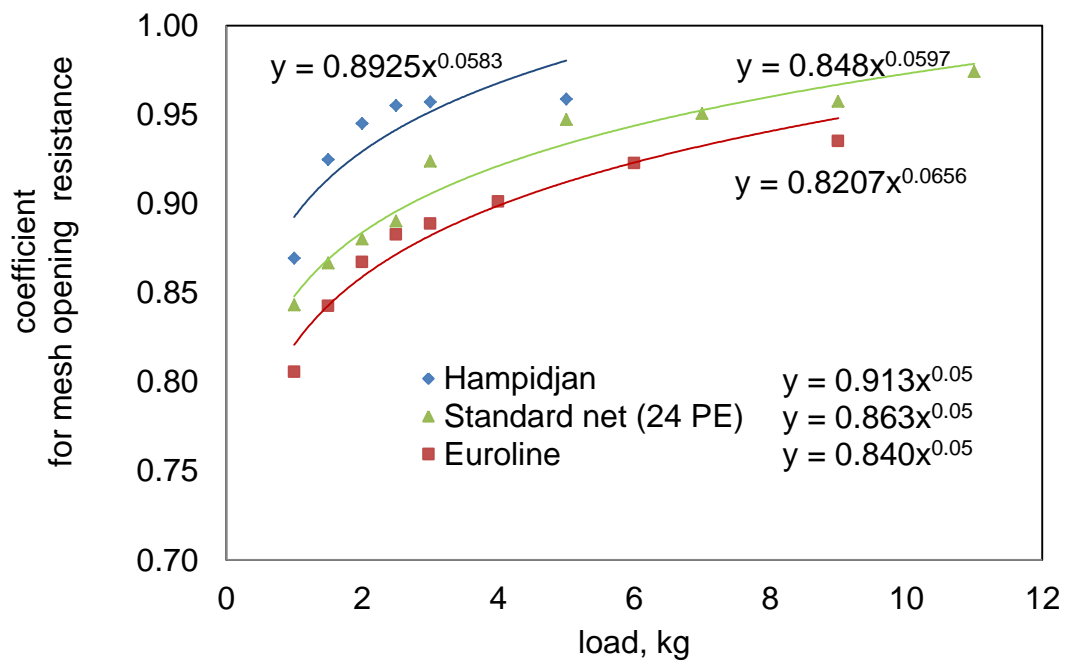
Fig. 3.10 Mesh resistance to stretch in the transverse direction for three samples (Table 2.1). A mesh opening coefficient (y-axis) is the ratio of mesh opening in the longitudinal orientation to mesh opening in the transverse orientation.

44

Table 3.3 A relative stiffness between the samples (Table 2.1)

Sample retail name	Trend line coefficient a of the function y=ax$^{0.05}$ (Fig. 4.10)	A relative stiffness increase
Ultracross Dyneema®	1.0	benchmark
Hampidjan Dyneex	0.913	10%
24 ply PE	0.863	16%
Euroline Premium Plus	0.840	19%

As no measurable difference was detected for Dyneema®, the coefficient *a* for this sample was assumed to be 1 in the linear function of *y=ax*, and the sample was perceived as a low bending stiffness benchmark. Then a relative increase in stiffness for Hampidjan, 24ply PE and Euroline can be said to be 10%, 16% and 19% respectively from the benchmark stiffness.

Flexural rigidity

Eq. 3.1 can be rearranged to give:

$$EI = f_x \left[\frac{x - a - m\cos}{4\left[\cos\left(\frac{\theta + \beta}{2}\right) - \cos\beta \right]} \right]^2 \qquad 3.9$$

Similarly, eq. 3.2 can be rewritten to estimate flexural rigidity using mesh opening and tension in *y*-direction. As seen from eq. 3.3 and 3.4, the horizontal and vertical hanging coefficients (u_x and u_y respectively) are interchangeable and can be expressed as follows:

$$u_x = (1 - u_y)^{0.5} \qquad 3.10$$

Combining eq. 3.5 and 3.10:

$$\frac{f_x}{(f^2 - f_x^2)^{0.5}} = \frac{u_x^2}{(1 - u_x^2)}$$

3.11

A horizontal component of the tension f_x then can be expressed as:

$$f_x = \frac{fu_x^2}{(1 - u_x^2 + u_x^4)^{0.5}}$$

3.12

Similarly, the vertical component of the tension f_y is:

$$f_y = (f^2 - f_x^2)^{0.5} = \frac{fu_y^2}{(1 - u_y^2 + u_y^4)^{0.5}}$$

3.13

Then, splitting the load f into f_x and f_y components with eq. 3.12 and 3.13, and using the measurements for mesh opening in x and y directions from the experiment, estimates for flexural rigidity were obtained from eq. 3.9. Knot shape deformation was not considered, and knot dimensions a and b (as specified in Fig. 2.13) were assumed to be constant. The results for flexural rigidity for one of the samples (24ply PE) are presented in Table 3.4, and Fig. 3.11 show results for all samples (except Dyneema®) in comparison with the results for flexural rigidity obtained by Sals et al. (2007) who suggested a linear relationship between flexural rigidity and twine linear density. As can be seen from Fig. 3.11, flexural rigidity data point scatter for a given liner density is very similar between two sets of data. In the present study, flexural rigidity figures vary within a netting sample by 14% from the mean value – such significant variation occurred as the analytical approximations by O'Neill (1996) considered an idealized twine which implied a number of assumptions, including that twine bent linearly, knots were of rectangle shape and twine did not elongate.

Table 3.4 Flexural rigidity figures for 24ply PE (parameters are defined in eq. 3.1).

f (kg)	f_y (kg)	f_x (kg)	β	ϑ	EI (Nmm^2)
1	1.0	0.17	-2.19	0.4	59
1.5	1.5	0.23	8.12	0.4	61
2	2.0	0.29	1.66	0.4	58
2.5	2.5	0.36	1.59	0.4	59
3	3.0	0.43	1.52	0.4	56
5	4.9	0.72	1.42	0.4	56
7	6.9	1.00	1.37	0.4	54
9	8.9	1.29	1.33	0.4	49
11	10.9	1.57	1.32	0.4	52
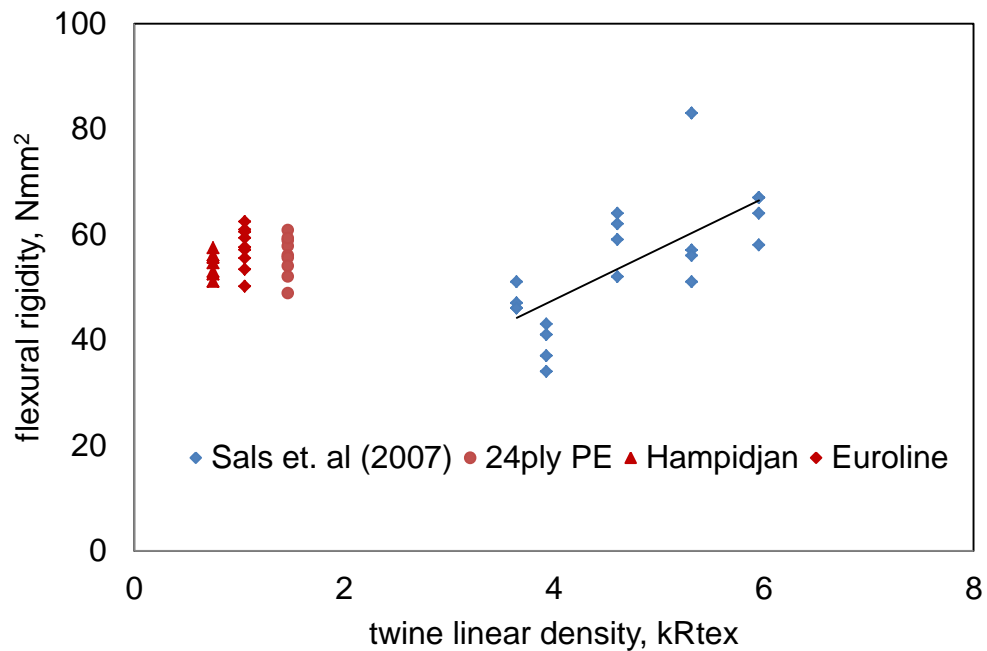
Fig. 3.11 Flexural rigidity as a function of twine linear density: data from Sals et al. (2007) (blue dots), and present study (red dots).

Sals et al. (2007) obtained flexural rigidity figures for net samples of a wide range of twine linear density - for very stiff nets with linear density between 5 and 20kRtex, a linear relationship between flexural rigidity and twine linear density was suggested. However, in a case of low twine linear density, a linear dependence of flexural rigidity on twine linear density is less pronounced (Fig. 3.11). When the results from the current study are considered together with Sals

et al. (2007) (Fig. 3.12) flexural rigidity can be said to be independent of twine linear density.
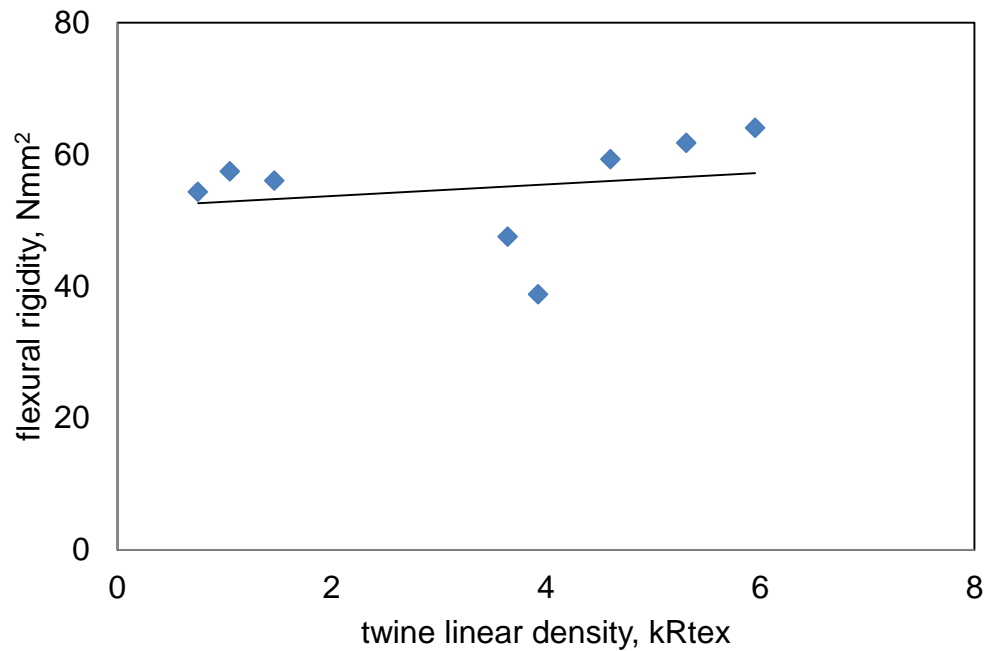
Fig. 3.12 Flexural rigidity as a function of twine linear density: averaged flexural rigidity data point for every sample from Sals et al. (2007) and present study.

3.6 Conclusions

An alternative method for obtaining netting flexural rigidity has been proposed. The method combines existing analytical approximation for an idealized mesh and experimental data for mesh opening in a net that is restrained between two hoops. The results indicate that a previously-suggested linear relationship between flexural rigidity and linear twine density is not applicable for cases of low twine linear density. Further experimentation is required to robustly define flexural rigidity as a function of linear density – this predictive tool will progress research on implications of fishing net stiffness: e.g. trawl drag and fishing gear selectivity.

Chapter 4

Prawn Net Drag due to Flexural Rigidity and Shape

4.1 Experimental goals

As described in chapter 1, current trawl scaling practices assume no material stiffness differences between the model and prototype. This assumption coupled with a practical limitation to scale a twine diameter linearly with respect to scale factor often results in significant drag overestimation from model tests (section 1.4). In addition, mixed results have been reported on parameters that determine the drag coefficient for low porosity nets exposed to flow at a low angle of attack (as discussed in section 1.5). The work presented in this chapter aims to address these shortcomings through development of the following methodologies:

- To establish a technique allowing prawn full-scale netting material usage in model experiments.
- To quantify drag variation for a typical prawn trawl with respect to netting flexural rigidity.
- To quantify the drag coefficient for a typical prawn trawl through the drag coefficient of plane net sheets.

4.2. Experimental methodology

Test objectives

The experimental objectives were to measure tension of four trawl models of various netting material stiffness over a range of flow velocities, and to acquire 3D shapes of these models.

Flume tank

The experiments were done in the flume tank at the Australian Maritime College, Beauty Point, Tasmania, Australia. The flume tank is 17.2 m long, 5 m wide and 2.5 m deep, constituting approximately 700,000 litres of fresh water. The flow is circulated with four contra-rotating impellers via constant speed hydraulic delivery pumps. The impellers are 1.2m in diameter and can run up to 200rpm, which delivers the flow speed of approximately 1.55m/s. A honeycomb installed upstream provides a uniform flow distribution. An 11m long perpsex window allows model observation from a side view.

Net design

Four ¼ scale models of 8 fathom Florida Flyer prawn trawls were built from full-scale netting materials that are commonly used by the industry and were assessed for their geometry and stiffness properties in chapters 2 and 3 (Table 2.1 and 3.3). The trawl models were built by an experienced trawl maker from Sterling Trawl Gear Services, QLD. The justification to use the Florida Flyer design for this study is provided in chapter 1, and the choice of netting material is explained in chapter 2. The net plan of the trawl model is shown in Fig. 4.1. On the left side of the net plan, taper sequences are shown, and the right side provides corresponding numbers of meshes produced by such taper sequences (for example, a wing taper of 1M3B (1Mesh 3 Bars) applied consequently 11 times creates 27.5 meshes in trawl width and 16.5 meshes in length). Hampidjan Dynex netting (model #3 in Table 2.1) was manufactured with double knots, which minimized the lateral mesh stretch by 16% compared to other model trawls, and required the incorporation of additional lateral meshes to maintain the standard frame-line length. Due to this, a steeper side taper of 1P5B (1 Point 5 Bars) had to be applied for this model in order to maintain a similar overall trawl length across all models. In addition, a number of wing tapers had to be modified for the Hampidjan Dynex model as shown in Fig. 4.1(b).
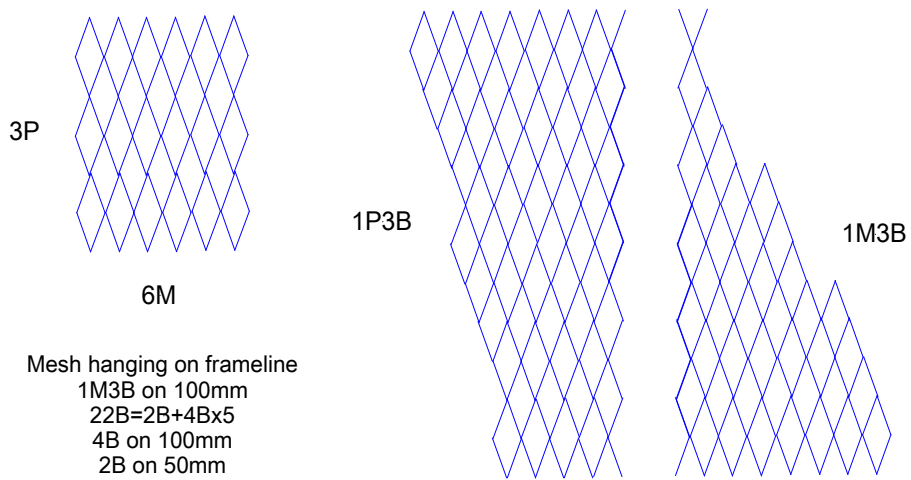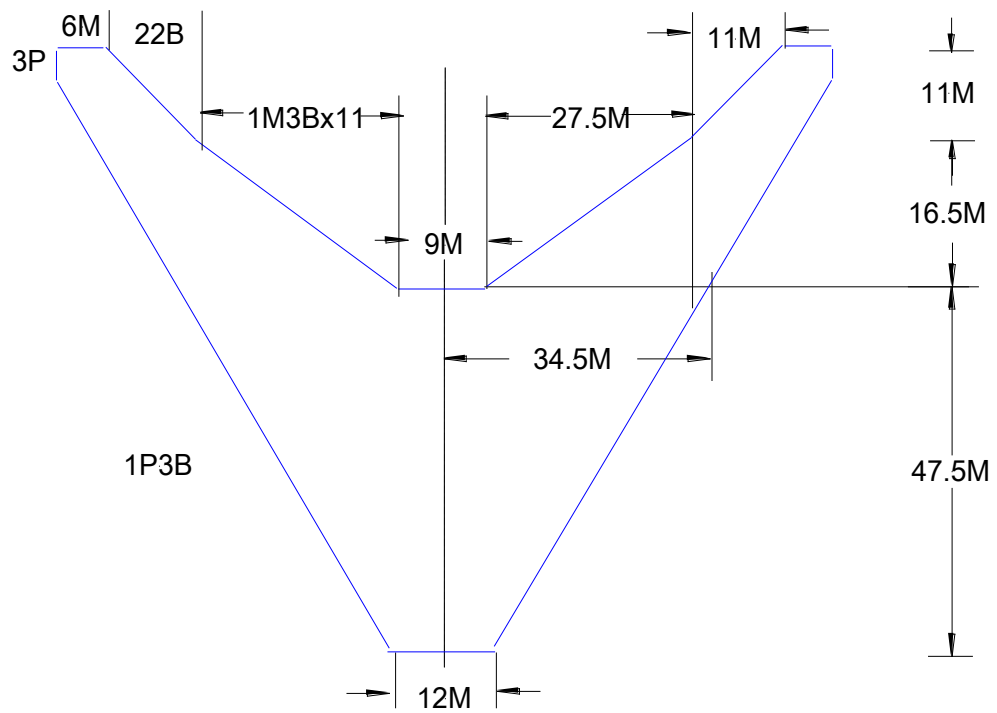
Fig. 4.1 (a) Net plan for ¼ scale 8 fathom Florida Flyer for all samples except
Hampidjan Dynex (Table 2.1)
Taper sequences are on the left side of the plan, and numbers of meshes
corresponding to these tapers are on the right. Top and bottom panels are
symmetric. P – Point, M – Mesh, B – Bar (definition is provided in section 1.3).

8M

22B

3P

1M3Bx11

11M

27.5M

11M

11M

16.5M

1P5B

35.5M

43M

14M

3P

8M

1P5B

1M3B

Mesh hanging on frameline
1M3B on 100mm
22B=2B+4Bx5
4B on 100mm
2B on 50mm
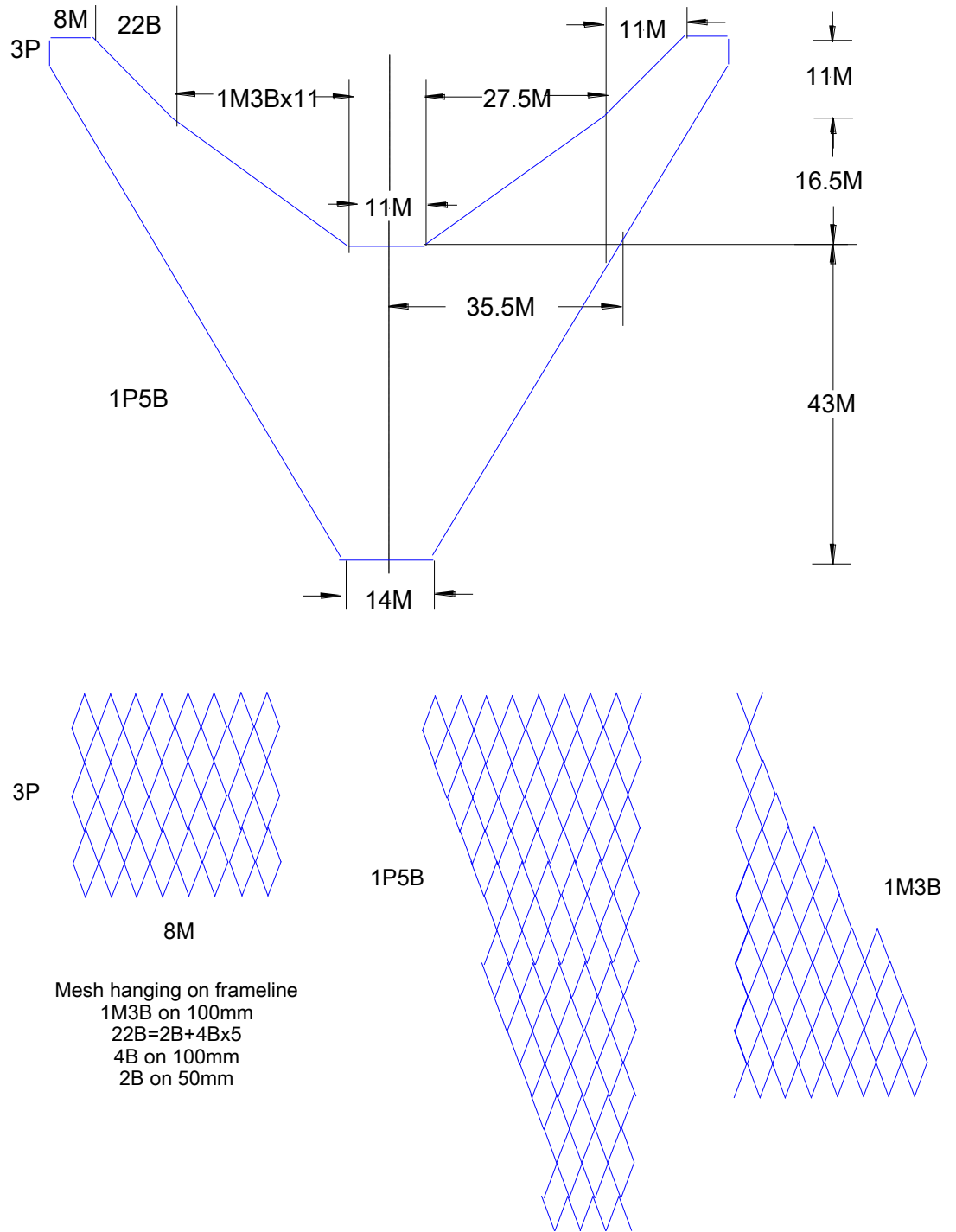
Fig. 4.1 (b) Net plan for ¼ scale 8 fathom Florida Flyer for the Hampidjan
Dynex model (Table 2.1)
Taper sequences are on the left side of the plan, and numbers of meshes
corresponding to these tapers are on the right.
Top and bottom panels are symmetric.
P – Point, M – Mesh, B – Bar (definition is provided in section 1.3).

load cells
skid
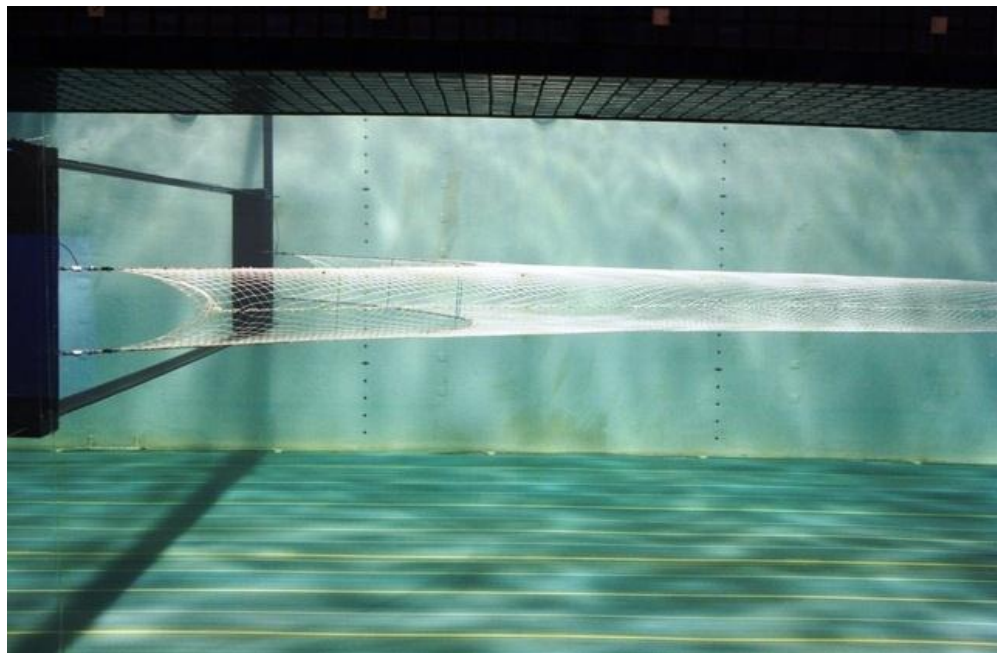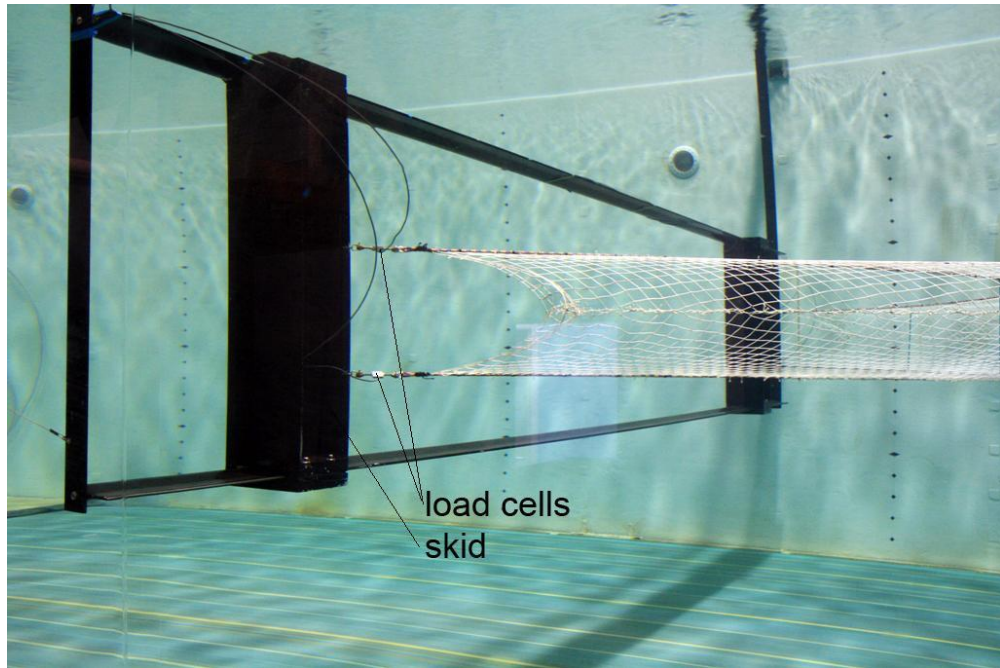
Fig. 4.2 Model attached to trawl evaluation rig and placed in the mid-stream.

Trawl scale

For a given flow condition (fluid speed and viscosity), net drag coefficient is a function of twine diameter, net porosity and an angle between the incident flow and net. It is often practically impossible to scale twine diameter and mesh size consistently, which results in a drag coefficient difference between the model and prototype. In the thesis, full scale netting was used to build model trawls. Full scale netting model experiments were done previously, but produced a drag measurement uncertainty due to full scale net stiffness variation across materials. In this work, a pre-stretch technique was developed to standardise net stiffness. In general, the obtained results showed no difference in the drag coefficients between the models of various stiffness. The usage of full scale netting in the model experiments coupled with the full scale flow speed maintained the constant Reynolds number between the model and prototype. Hence, the full scale drag can be directly predicted through an overall trawl size scale. The experiments with nets of other overall trawl size scales would not be beneficial - the work of Hu et al. (2001) showed a negligible drag difference in respect to an overall trawl size scale. Field experiments would return a minimal practical value in the scope of the presented research for the following two reasons: (1) field trials drag data are heavily biased by uncontrolled environmental factors (i.e. currents and uneven sea floor); (2) field trials are complimentary to model test only when the research focuses on operational implications and catching performance of new trawl systems.

As this study focused on the relative drag between various net stiffness models, a number of gear design simplifications were applied to exclude features that were hard-to-control for their consistency. These simplifications are discussed below.

Model positioning in the CWC

A model trawl tow was simulated by moving the body of water along the tank while the trawl remained stationary. While fishing, a horizontal trawl opening is maintained with otter boards. However, the otter boards produce variable opening due to a wide range of hydrodynamic factors (Sterling 1998). Hence for a more controlled test, the trawl model was attached by the four end points of

the upper and lower frame lines to a trawl evaluation rig (TER) as shown in Fig. 4.2. The TER was an aluminium rectangular frame where the two vertical side slides and can be firmly fixed at any desired location with four bolts. Each connecting point contained a load cell with U-shape shackles on both ends: on one end it connected the load cell with the TER, and on the other with the trawl model frame line.
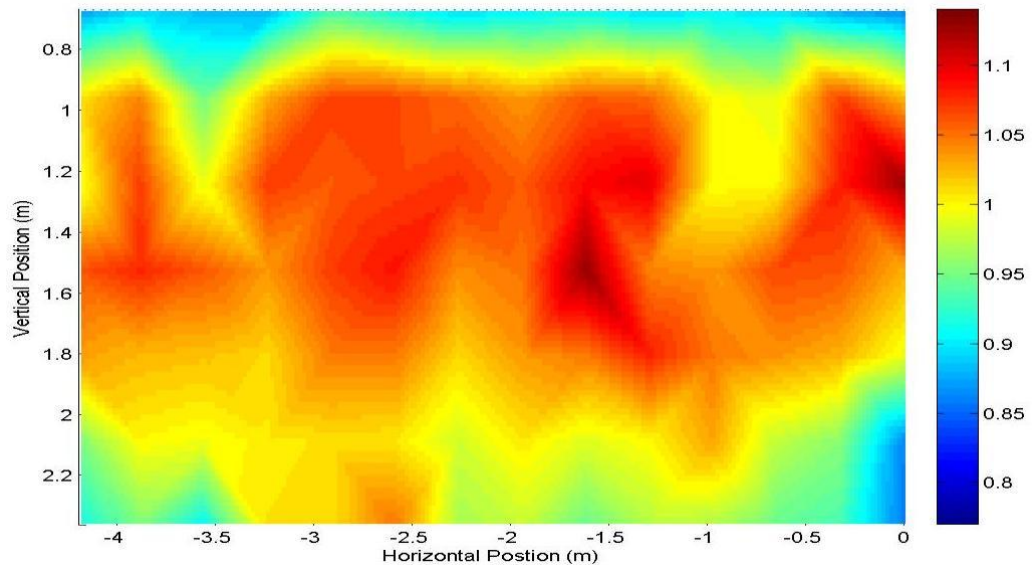
Fig. 4.3 A sample of flow distribution in a flume tank cross-section (Kok 2010); the legend bar shown on the right presents flow speed in m/s.

At sea the trawl is towed on the sea-bed. Kok (2010) surveyed flow distribution in the flume tank at the Australian Maritime College. Fig. 4.3 presents a sample of flow distribution in a tank cross-section with the hydraulic pumps set to 125rmp, which produces the flow of approximately 1.05m/s. The horizontal axis is a width of the tank, the vertical axes is a depth of the tank, and the colour bar on the right side is a flow velocity legend. The flow at the middle section depth wise is distinctly steadier compared to the bottom of the tank. Thus to avoid noise associated with less steady flow of the bottom section, the models were tested in the mid-section and no ground forces applied since ground force simulation was outside the scope of the research. In an off-shore trawling situation, a ground chain is attached along the front line of the bottom panel. In these experiments, a ground chain was not attached to the model as it would

cause the trawl to become grossly out of shape when tested in mid-water and greatly increase the tension along the lower frame line and through the bottom panel. In addition, the chain would merely represent a constant drag figure across the models that to be subtracted from the total measured drag for netting drag analysis.

Horizontal and vertical model trawl openings

In industry it is desirable to operate prawn trawls at a high spread ratio to cover the maximum area per-unit-time and catch the maximum amount of target prawns (the spread ratio is defined in Fig. 1.11). Wakeford (1999) showed that an increase in the spread ratio from 83% to 87% caused a significant tension transfer to the headline from the footrope, which created operational difficulties. In addition, a higher spread ratio results in a greater twine area exposed to the flow at a larger angle of attack, which causes an overall higher trawl drag. The optimal spread ratio is a complex question and depends on rig type, trawl design and the efficiency of the otter boards used. In industry a spread-ratio of 80% is often used and was chosen for the flume tanks tests – this provides a high spread without unwanted implications. The distance between the lower and upper panels (vertical mouth opening) was set at the TER to 226mm. As the overall size of the models were at a ¼ scale of the prototype, a 226mm vertical opening in the tank tests equated to an about 1m at full-scale. The vertical mouth opening does not have to be more than 1m since prawns are typically located in the lower one meter of the water column.

As mentioned in chapter 1, in prawn trawl design the forepart of the top panel is often extended forwards compared to the bottom panel. This design feature prevents prawns from jumping above the trawl. Each net panel is symmetric in respect to the axis that aligned with the direction of towing. Because of this, it is conventional to show half of each panel only on a net plan. As seen from the net plan from the current study (Fig. 4.1), the top and bottom panels were the same and produced a symmetric trawl about the horizontal central plane, in general. This simplification, which gives rise to no lead-ahead in the trawl, allowed the vertical opening around the frame-lines to be fixed by applying four equally spaced 3mm-wide fibre-glass struts along the frame lines (Fig. 4.4). This

methodology standardised the vertical opening in the mouth of the trawl against the effect of varying vertical knot forces between the models (i.e. knots pushing the panel in/out depending on knot construction and orientation).
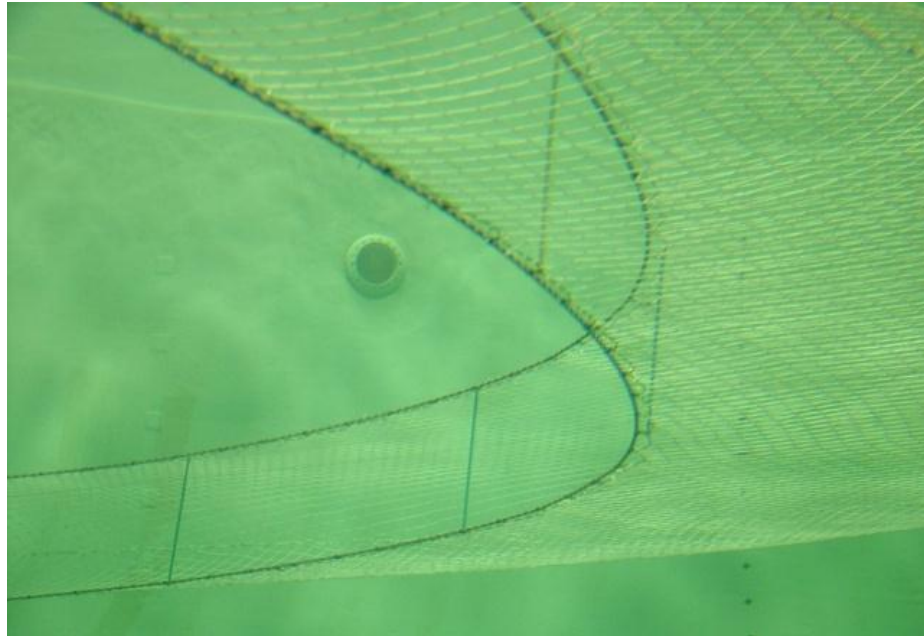
Fig. 4.4 Forepart of model-trawl during testing showing vertical struts fixing the vertical opening at the mouth.

Cod-end

Each trawl was tested without a cod-end. Cod-ends are netting bags that collect the catch in the aft section of the trawl whilst trawling; and represent much stiffer netting sections compared to trawl panels so they retain the catch. A review of previous flume tank work involving full-scale netting cod-ends (Flesser 1994) showed that the flow is not strong enough to overcome a residual shape of the cod-end and hence the measured tension was arbitrary. Thus, it was deemed prudent to exclude this source of drag variation. Instead, a 1mm thick thread was laced through the last trawl meshes to ensure a constant round opening. The circumference was equal to the distance that would occur in the case of the aft part of the trawl to be attached to a 24 mesh-width cod-end.

Model pre-stretch

To quantify the effect of flexural rigidity on drag, each trawl was pre-stretched longitudinally and transversely respectively before measuring the drag from two independent tests in the flume tank. The stretching process involved dividing the trawl into about 40 sections and a slight manual pull for each section (in a longitudinal or transverse direction, depending on the case). To check variation due to the arbitrary nature of the technique, a replication was run for the Euroline Premium Plus (sample #4 in Table 2.1). This implied testing the sample in the flume tank on its drag performance in the alternating pre-stretch directions four times (twice longitudinally and twice transversely).

Data acquisition

The flow velocity was recorded with an electro-magnetic probe located 7 m upstream of the model, 1.25 m below the free surface on the centre line of the test section. The positioning of the velocity probe 7m upstream from the trawl evaluation rig was reasonable. The survey of flow distribution in the flume tank (conducted by Kok, 2010) showed that velocity flow remains constant across the tank sections and a significant velocity gradient is present depth wise only. The model tension was measured with four load cells of 20kgf capacity each and $\pm$ 0.05 kgf accuracy. The load cells were calibrated and zeroed at the beginning and end of testing. The total trawl tension for a given model and flow speed was estimated through a linear summation of the 4 load cell readings. Data was sampled at 50 Hz. For each trawl-net scenario the flume tank propellers were set sequentially to four operating conditions: 200, 180, 150 and 120 rpm (the propellers operating at 120 rpm produce flow of about 0.95 m/s). Data for each speed regime was recorded for at least 5min to acquire statistical significance. For the samples #1, 2 and 4 (Table 2.1) measurements were also recorded for flow speeds in an ascending order (from 120 to 200 rpm) to check for consistency in measurements.

Drag and in-pull components

The total measured tension T was produced by the in-pull force F_{in} that must be overcome to keep the trawl open and the drag force F_d – the trawl resistance

while towed through the water. As seen from the sketch (Fig 4.5), the relationship between the tension-components and tension is determined by an angle θ between the frame line and flow direction. The drag component F_d was derived as shown in eq. (4.1).

$$F_d = T \cos \theta \qquad\qquad 4.1$$
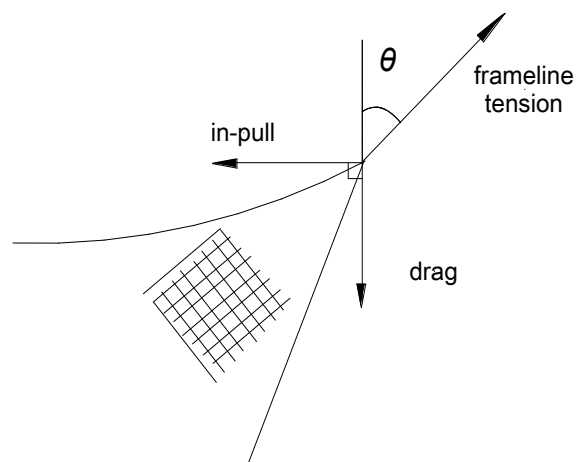
Fig. 4.5 Force vector breakdown.

The wing-end angle θ used in eq. 4.1 was the average of measurements from each tested model. A single average value was used because the low accuracy of the angle measuring system. In addition, there was no theoretically-based expectation that wing-end angles would vary between trawl-net scenarios. The average figure stabilises the error and does not add noise into the data by applying local measurements of the wing-end angle to respective tension measurements. Netting-only drag was determined by tarring off the drag for the ropes and the four struts fixing the vertical opening from the total drag component F_d. The rope and strut drag was estimated theoretically by assuming circular cylindrical cross sections.

Twine area

A twine area of 1 mesh A_{mesh} was calculated as shown in eq. 4.2:

$$A_{mesh} = 2d(l - 2a) + 2ab \qquad\qquad 4.2$$

where d is twine thickness, l is mesh size, a and b knot dimensions as specified in Fig. 2.13 and Table 2.1. Twine area for the trawl model was estimated by multiplying the twine area of 1 mesh A_{mesh} and a number of meshes in the model n. The number of meshes n was estimated from the net plans (Fig. 4.1). The results are presented in Table 4.1.

Table 4.1 Model trawl twine area.

	Retail name	1 mesh twine area	Total number of meshes in model	Trawl area
		A_{mesh}	n	A
		(mm^2)	-	(m^2)
1	24ply Polyethylene	195.0	1422	1.109
2	Ultracross Dyneema®	128.1	1422	0.728
3	Hampidjan Dynex	139.4	1395	0.832
4	Euroline Premium Plus	168.1	1422	0.956

As mentioned above, the lateral mesh stretch of Hampidjan Dynex (sample #3 in Table 4.1) was 16% lower compared to other model trawls. In order to maintain a constant frame-line length and similar overall lengths across the models, additional lateral meshes were included, and steeper cutting tapers were also applied (as shown in Fig. 4.1), which resulted in a total number of meshes for Hampidjan Dynex being slightly different from other models. In fish farm installations where net cages are positioned in a row, the speed of the flow reduces as the flow proceeds through the cages. Flow reduction (also known as shadowing) is due to energy losses required for the flow to first decelerate and then accelerate as it approaches and exits the net. Hence, it is sensible to assume that a relatively large net exposed to the flow at a low angle of attack may also create a flow shadowing effect which modifies an overall net drag. In this work, if overall trawl sizes varied between the models, it could introduce significant

flow shadowing variation which would create an unknown variable in the measured drag.

Trawl shape capture

A volume of work has been conducted previously to simulate net shape. Due to the complexity arising from coupling a flying shape and hydrodynamic forces, calculation programs for a simple net shape and trawl two-dimensional shape have been developed only up to date (O'Neill, F G. & Priour 2009). In this work, trawl shape was captured with three still image cameras (Canon EOS 1000D, EF-S 18-55mm lenses): two cameras were installed along the observation window and one camera was mounted on the towing carriage above the model (Fig. 4.6). Each camera was connected to PocketWizard[©], a radio signal receiver and camera trigger device. The fourth PocketWizard[©] served as a transmitter to send a triggering command to the receivers which enabled images to be taken simultaneously. To standardise lenses and observation window distortion, cameras were calibrated using a frame shown in Fig 4.7 (geometric parameters of the frame are specified in Appendix II). To eliminate surface disturbance while image capturing, a Perspex window framed in a wooden structure (as shown in Fig. 4.6) was positioned over the trawl model. Plastic spherical beads of 3mm each were marked throughout the left side of the top panel and served as target points (www.winanalyze.com). The WinAnalyze[©] software package was used to calibrate the cameras and to determine the coordinates of each target points. The trawl shape was fragmented in to plane net sheets. The angle between the flow and each panel was determined with the cross dot product of two vectors (AB and CD as shown in Fig. 4.6). The weighted average angle between the incident flow and trawl model was determined as shown in eq. 4.3:

$$\bar{\alpha} = \frac{\sum \alpha_i A_i}{\sum A_i} \qquad\qquad 4.3$$

where α_i is the angle between the flow and the panel and A_i is twine area of the panel.
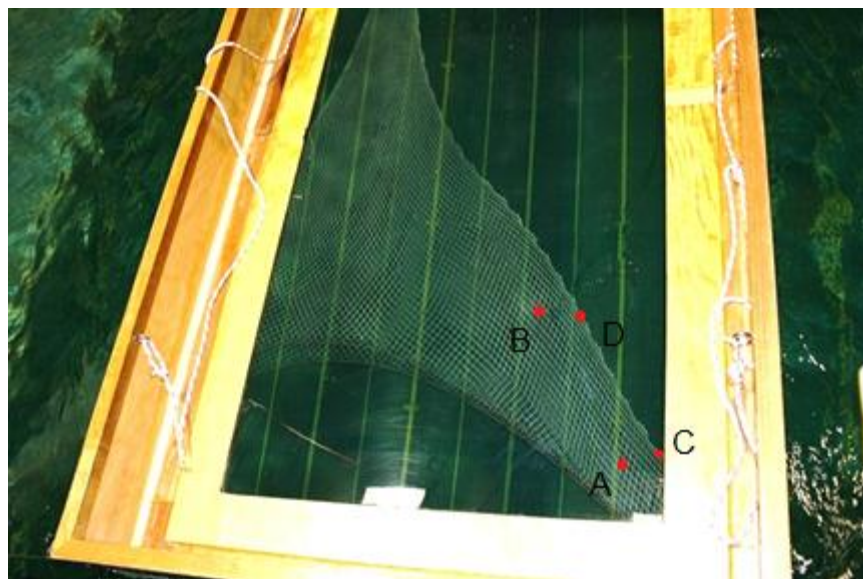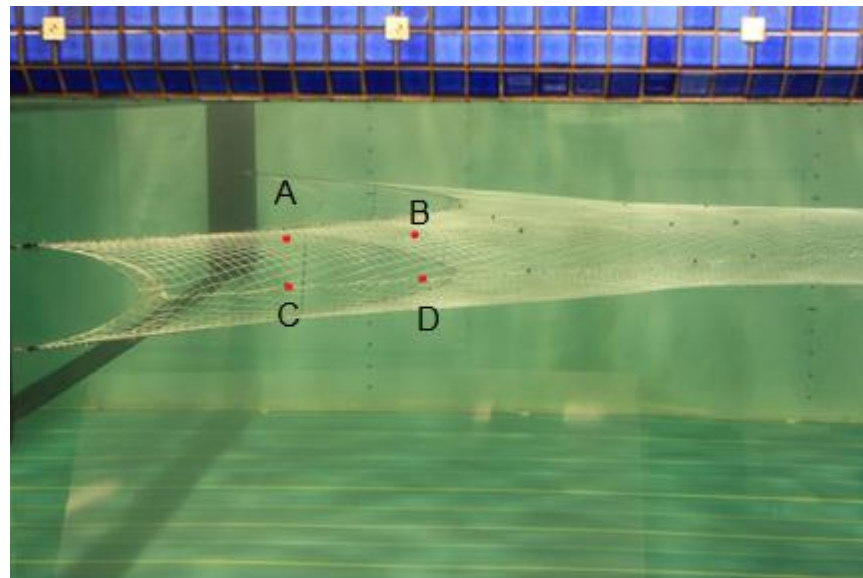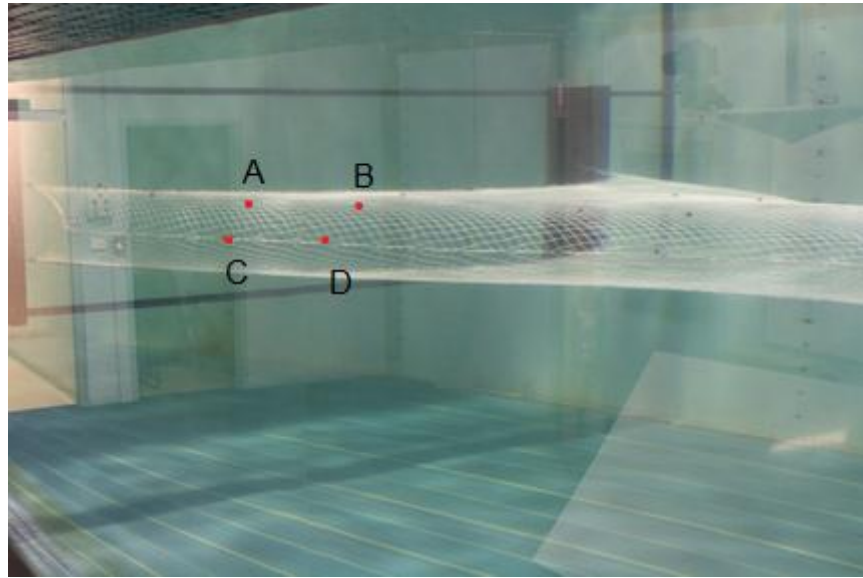
Fig. 4.6 Trawl shape captured with side view and top cameras.

Fig. 4.7 A camera calibration frame - top view (in analysis, the image taken through the boat Perspex window was used to account distortions produced by the window).

The weighted angle estimation allowed (1) ensuring all models were of the same flying shape and (2) to compare the netting drag coefficients from the present study with previously published results on drag coefficient of nets at a low angle of attack to the flow.

4.2. CWC eperimental results and discussion

Data accuracy

Samples of raw data are shown in Fig. 4.8. Each point represents an average of 50 readings over a second. As mentioned above, data for each flow velocity was recorded for at least 5 min. As the number of recorded data points varied between runs, 300 points only were taken for each set to retain statistical consistency (Fig. 4.8b). The experiments were to be quasi-static, but flume tank propellers do not maintain a completely steady rotational speed and cause flow speed fluctuations that are especially pronounced for lower speeds (Fig. 4.9 illustrates rotational performance of each propeller for four sets of rpm - 200, 180, 150 and 120). However, as illustrated in Fig. 4.8 (b), drag measurements were in correlation with flow variation (the correlation coefficient was greater than 0.998). Net drag variation with respect to velocity data is presented in Fig. 4.10. For higher velocities of approximately 1.42 and 1.60 m/s occurring at 180

and 200 rpm respectively, the drag of the trawl does not appear to be dependent on flow speed within the test condition.
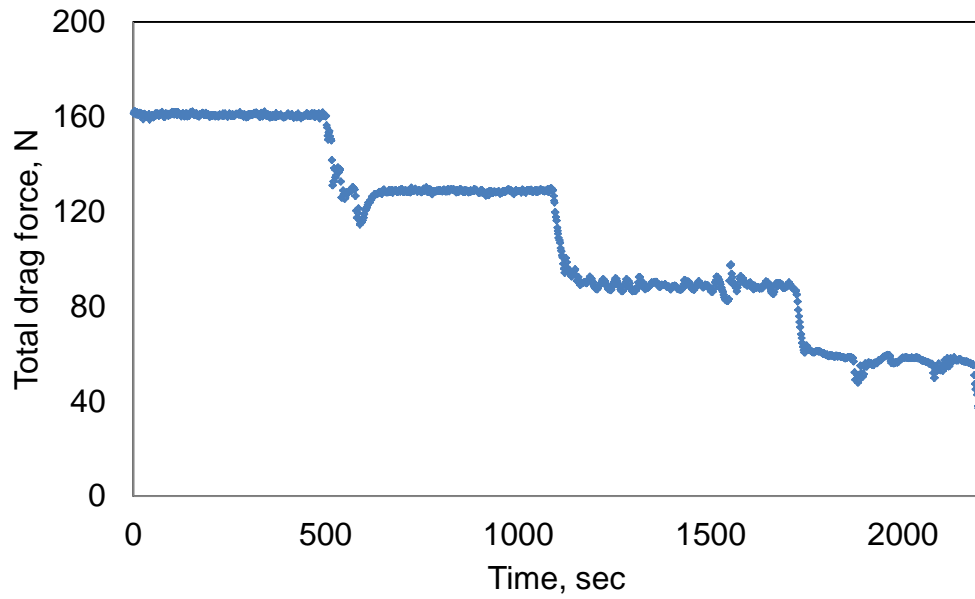
Fig. 4.8 (a) Samples of raw data: continuously-recorded drag measurements for four sets of flow speed and transient (decelerating) flow regimes.
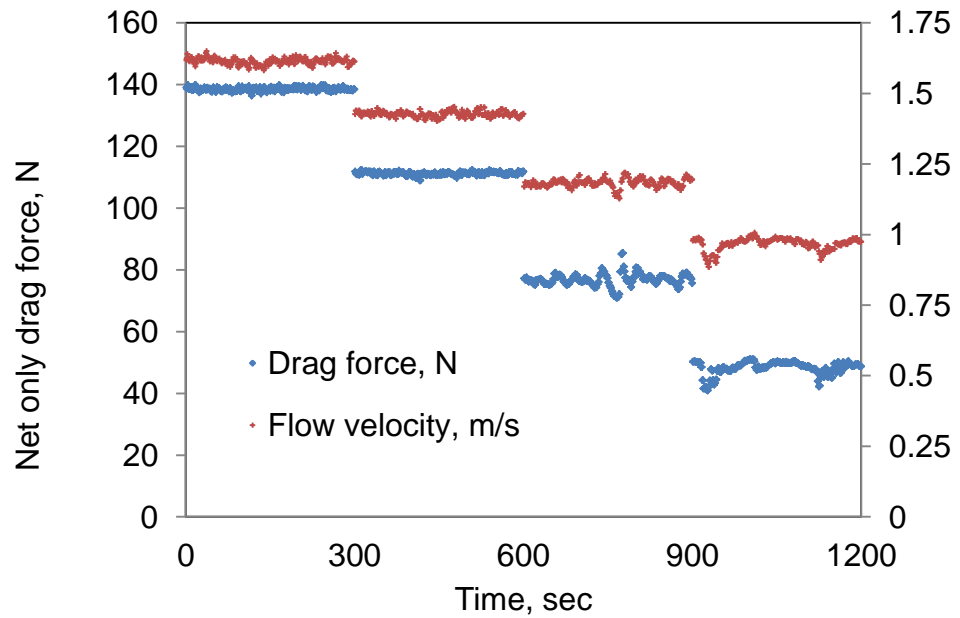
Fig. 4.8 (b) Samples of raw data: net drag in correspondence to these four velocities with 300 time points only for each set.

For higher velocities, the drag of the trawl does not appear to be dependent on flow speed within the test condition. This was caused by the introduction of small-scale turbulence in the flow at higher speed that resulted in large velocity variations at any given point such as velocity measurement point, while the trawl experienced the average velocity in the tank across its entire surface area, which remained relatively fixed and caused the trawl's drag to remain quite steady despite reasonable variations in measured local speed at the speed log. In contrast at the lower tank setting, variation in measured speed related to variations in propeller rpm that caused large scale variations in flow velocity that operated over the whole trawl surface and caused associated variations in trawl drag. Hence, a temporal average to represent flow rate (the flow across the section of the trawl) is a legitimate assumption as the turbulence seen in the velocity is not correlated in the trawl.

In all cases the exponent of the power regression is slightly higher than 2 (Fig. 4.10), showing that hydrodynamic drag increases slightly more rapidly with speed. This can be explained by the fact that the nets are generally "inflating" with speed, due to the bending resistance of the mesh elements, producing increasing exposure of netting elements to the flow.

A regression analysis proved a strong relationship between the measured drag and velocity (P-value was less than 0.05). A random nature of residual distribution for the drag for a given set of flow velocity (Fig. 4.11) shows a strong dependence between the measured drag and flow velocity. When drag and flow velocity are averaged for each flow speed, the resulting values illustrate a high level of data consistency (the results for one of the trawl models shown in Fig. 4.12 and 4.13). The confidence level for the data fit obtained from the regression analysis was greater than 99%. As the level of error is very low, for illustrative purposes, a sample of error bars in Fig. 4.13 has been magnified. A standard deviation for an individual load cell was about 7.77 ± 0.03 kgf (for Standard net – L tested at 200rpm flow) - this number was constant between load cells, but for a given load cell the error marginally fluctuated with flow speed change.
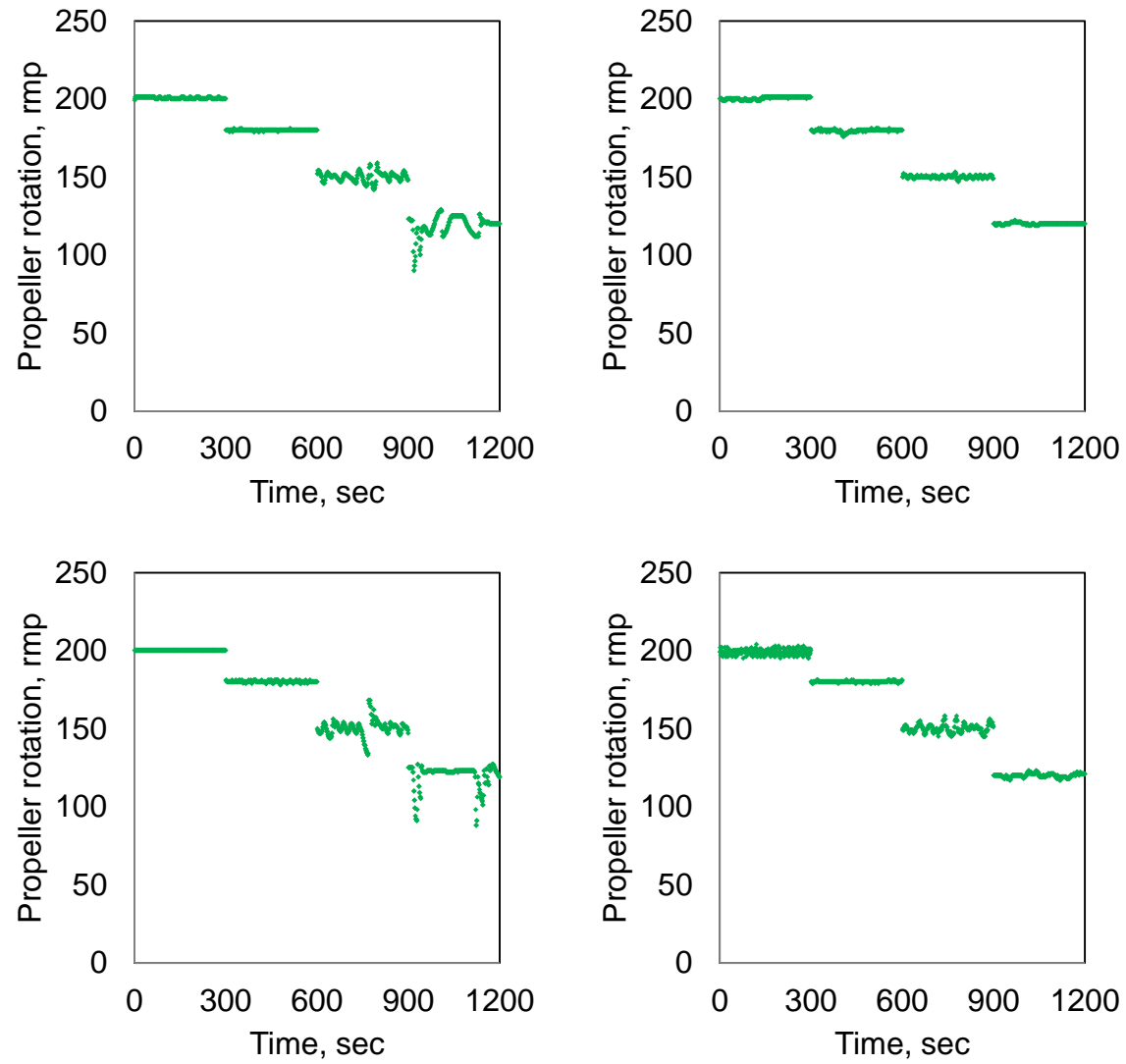
Fig. 4.9 Propellers' performance: #1 and #2 on top, #3 and #4 on bottom.
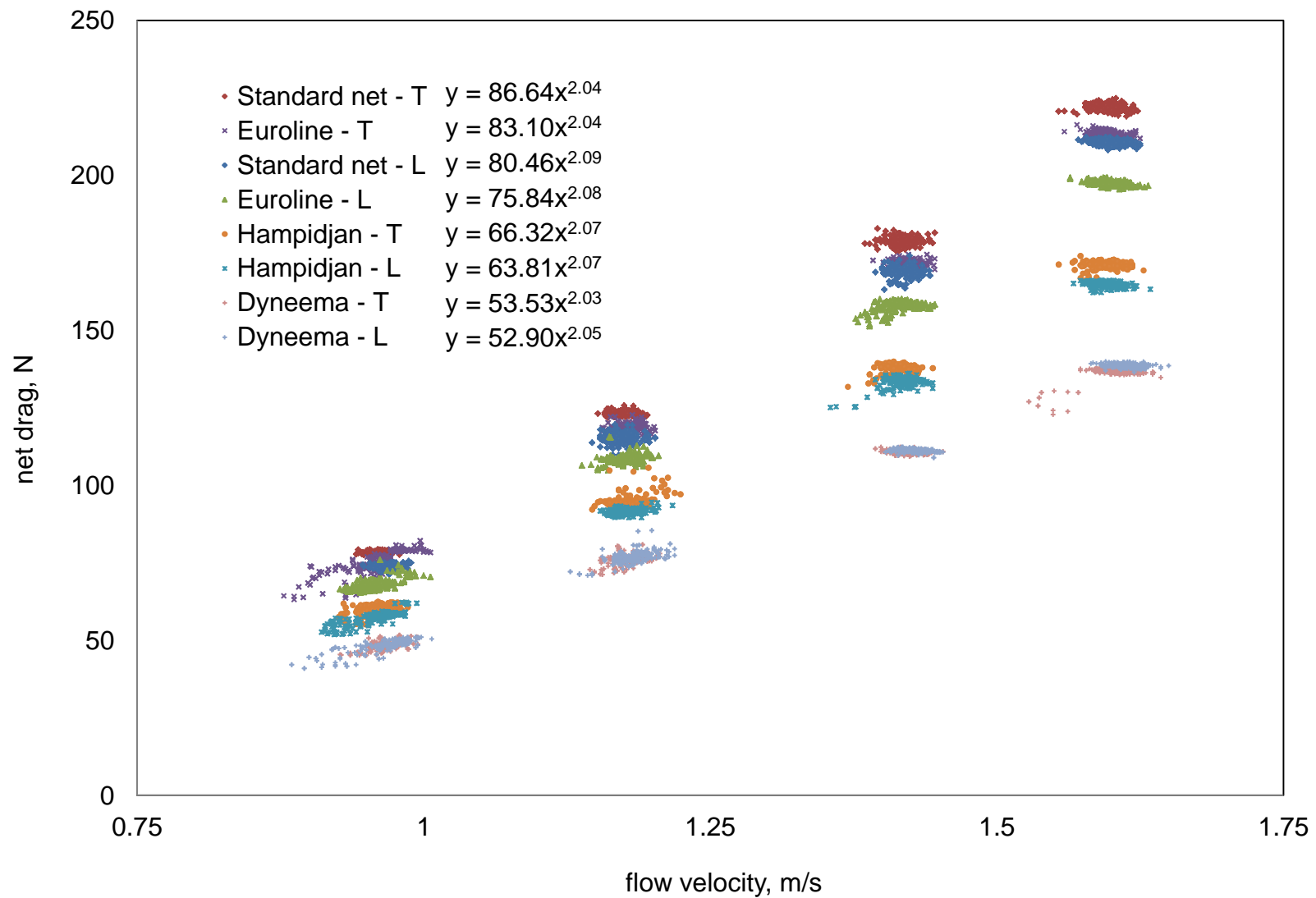
Fig. 4.10 Net drag vs. flow velocity (L – pre-stretched longitudinally, T – transversely).
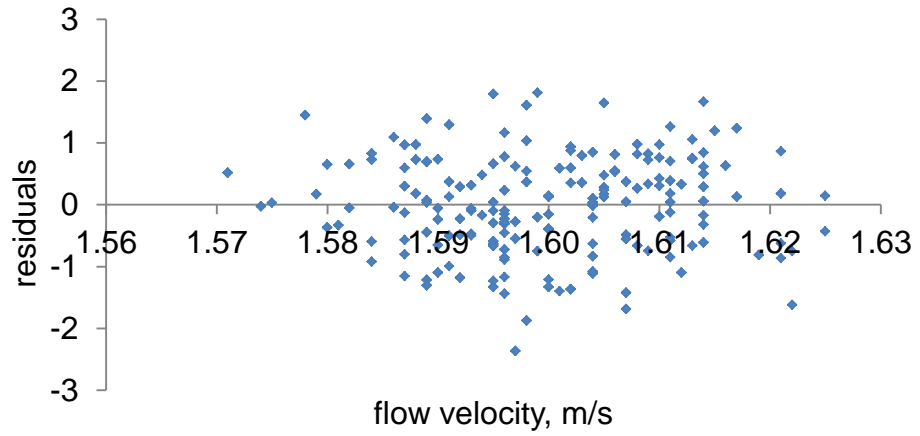
Fig. 4.11 Drag residual distribution.
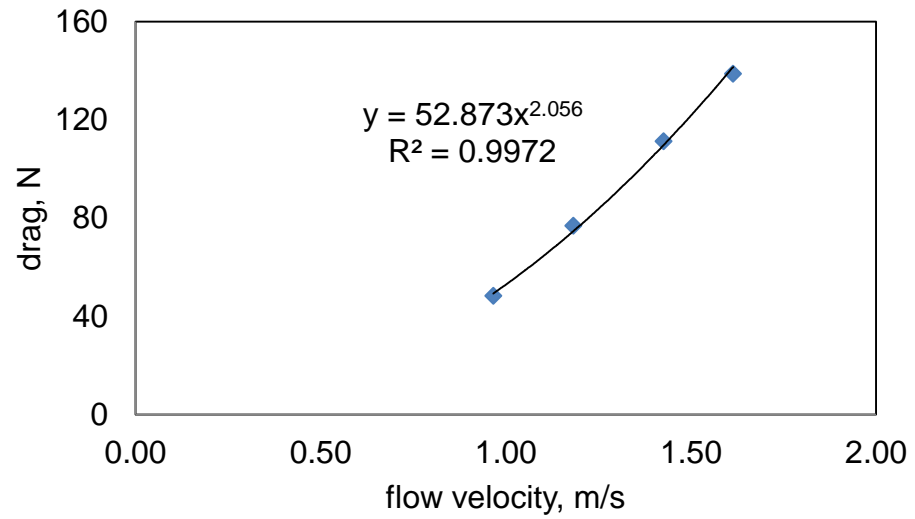
Fig. 4.12 Drag vs. flow velocity – averaged values.
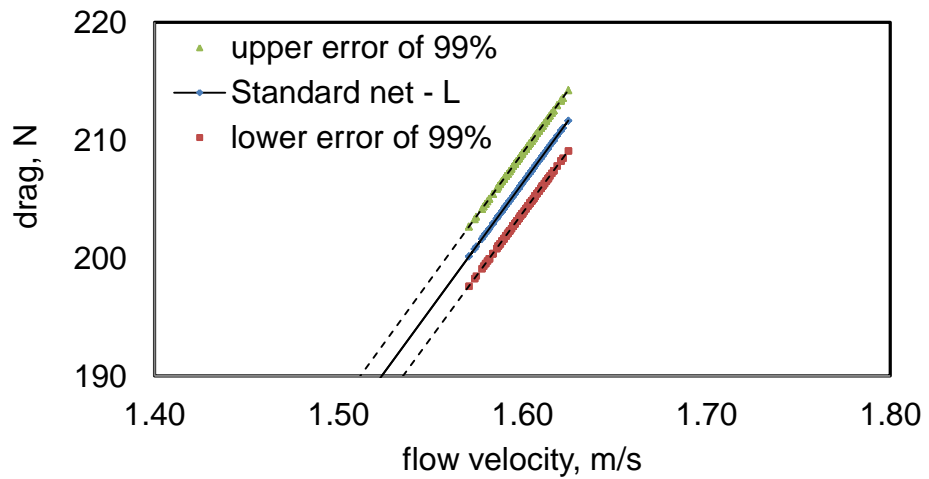
Fig. 4.13 A sample of error bars with 99% confidence.

As net pre-stretch was of an arbitrary nature, a replication test was run for model #4 (Table 2.1) to check a level of results consistency from the method. The replication test involved measuring the model drag from four independent tests in the flume tank in the alternating pre-stretch directions (twice longitudinally and twice transversely). The drag difference between the runs was less than 0.5%. Such a high level of repeatability was probably due to the intrinsic spring characteristic of the netting to adjust to the pre-stretch, and once the model was exposed to a hydrodynamic load, the memory for initial shape governed residual bending of the individual twine.

A model pre-stretch effect on drag

Based on a dimensional analysis principle, drag is proportional to the second power of flow velocity. The trend lines shown in Fig. 4.10 depart slightly from the theory in that the drag increases more rapidly than expected with increasing flow velocity. This could be due to net inflation under increasing hydrodynamic load which resulted in a higher twine area exposure to the flow. A linear regression analysis was applied using a quadratic relationship between velocity and drag. The associated coefficient in the model was used as a single performance indicator for each case in respect to drag. A modified set of drag vs. velocity graphs is presented in Fig. 4.14.

As can be observed from Fig. 4.14, a drag difference between a model being stretched in the longitudinal and transverse directions increases as netting stiffness of the model increases (the results for netting stiffness are presented in Table 3.3). Dyneema®, which was shown in chapter 3 to have no bending resistance, was barely influenced by the pre-stretch process – the drag difference between two types of pre-stretch was 0.5% (drag data for the pre-stretch in the longitudinal (L) and transverse (T) directions overlap). The model built from Hampidjian had a 5.5% drag difference between the two types of pre-stretch while a stiffness increased by 10%. The standard net (24ply PE) was 16% stiffer and the drag difference between the pre-stretches was 6% (the results for this model are not shown in Fig. 4.14 for

illustrative purposes – as can be noted from Fig. 4.10, the drag results for the Euroline model stretched in the T-direction overlap the data for PE model stretched in the L-direction). The stiffest model was built with Euroline netting which had twine bending resistance of 19% higher compared to no-bending resistance Dyneema[®], and a difference in drag measurements was the most pronounced – 8.0%. Fig. 4.15 summarizes the results for a relative drag increase caused by an increase in netting stiffness. Fig. 4.15 shows a relative drag increase for four models tested caused by the pre-stretch process: each point presents a relative netting stiffness measured from the stiffness experiment and drag difference between the trawl model stretched in longitudinal (L) and transverse (T) directions.

A low number of data points in Fig. 4.15 does not allow assumptions on linearity of interpolation and extrapolation. However, as the net becomes stiffer, a sharper rise can be seen in the drag difference with a relatively small change in flexural rigidity. It is sensible to assume that the curve will become even steeper with further flexural rigidity increase. Similarly, on the left side of the graph, a steep drop can be expected as the net becomes soft enough that the flow easily overcomes pre-stretch.
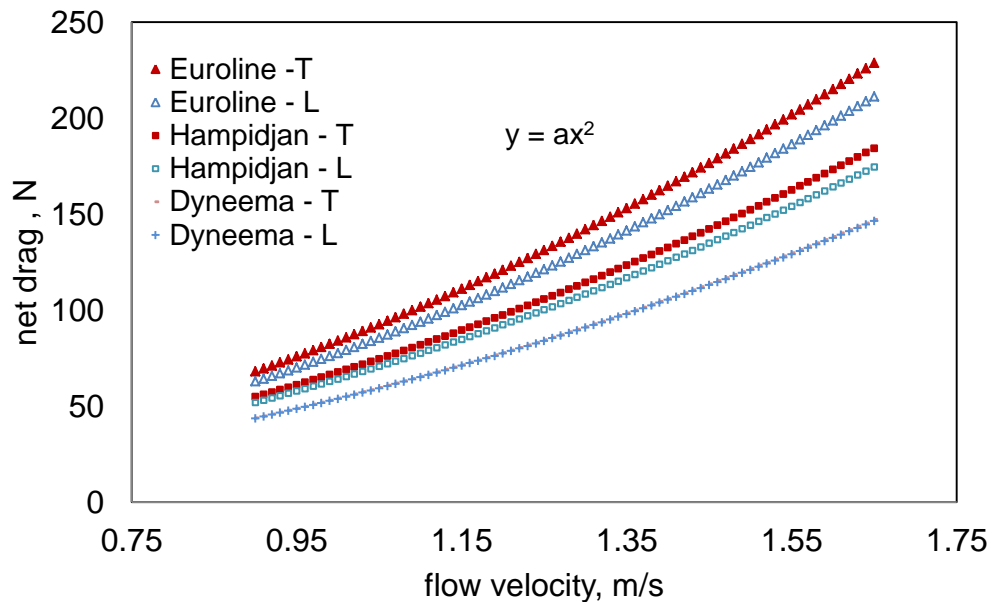
Fig. 4.14 Drag vs. velocity – a power exponent is adjusted to the figure of 2. A drag difference between transverse (T – red dots) and longitudinal (L – blue dots) pre-stretch increases for a given sample as the model stiffness increases
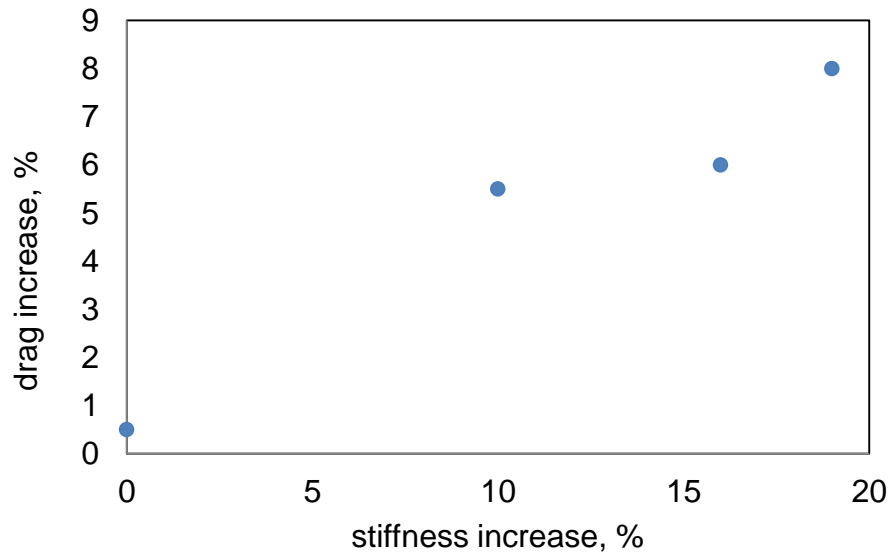
Fig. 4.15 A relative drag increase between two types of pre-stretch (L and T) due to a change in netting stiffness.

A drag increase due to a change in netting stiffness shown in Fig. 4.15 indicate an extent by what the drag vary within a model depending on the type of applied pre-stretch: by 0.5 % for soft Dyneema$^{®}$ and by up to 8% for stiff Euroline. However, as shown in Table 2.1 twine area varied between the models mainly due to different twine thickness and knot dimensions. Thus, to adequately quantify an effect of twine stiffness on the drag between the models, the drag was non-dimensionalised, and presented through the drag coefficient as a function of the Reynolds number.

The definitions of the drag coefficient and Reynolds number are not now included and the discussion is as follows (starting from p. 71):

A conventional geometric parameter for the Reynolds number in application to fishnets has not been established. The Reynolds number for a circular cylinder represents a ratio of inertial and viscous forces:

$$Re = \frac{Ud}{v} \qquad 4.4$$

where U is flow velocity, v *is* kinematic viscosity and d is cylinder diameter.

In application to trawl models, previous scientific approaches considered mesh size (Fridman, 1973), twine thickness (e.g. O'Neill (2003) and overall size Hu et al. (2001) as a length parameter for the Reynolds nubmer. Mesh size in part determines net porosity, and in this regard affects the drag coefficient – a less porous net experiences a higher drag due to increased energy losses as the flow goes through a finer mesh screen. To account for a mesh size effect on the drag coefficient, netting porosity can be incorporated into the Reynolds number in a way that corrects the local velocity driving the boundary layer flow around the twine elements (i.e. the ratio of dynamic forces to viscous forces) and how this characterizes the flow separation (Fridman, 1973). Twine thickness was chosen as a length parameter for the Reynolds number while mesh size and overall size were constant between the models. To account for flow energy losses to decelerate and accelerate as the flow travels through the net, the Reynolds number was calculated based on the local velocity $\bar{U}$ which was modified from the upstream velocity U by net porosity (White, 1991):

$$\bar{U} = \frac{U}{(1 - S_d)} \qquad 4.5$$

The netting solidity S_d across the samples varied from 0.10 to 0.15, which produced a corresponding change in the Reynolds number (eq. 4.4) when the local velocity was calculated as shown in eq. 4.5

The drag coefficient was calculated as shown in eq. 4.5:

$$C_d = \frac{F_d}{0.5\rho A \bar{\bar{U}}} \qquad 4.6$$

72

The drag coefficients as a function of the Reynolds number for one of the samples that was tested in longitudinal and transverse pre-stretch are shown in Fig. 4.16. The longitudinal stretch lead to less twine being exposed to the flow compared to the transverse stretch which produced a drag difference between two cases. The drag coefficient for the model that was stretched longitudinally increases slightly with increasing Reynolds number, while the drag coefficient for the model that was stretched transversely also shows a slight but less pronounced increase with the Reynolds number change. This could be explained by the fact that the model tended to inflate as the hydrodynamic load increased. The model inflation caused more twine exposure to the flow which slightly increased the drag. The transversely stretched model showed less relative drag increase in respect to the Reynolds number (compared to the longitudinal case) as the stretch process mechanically inflated the trawl to a maximum extent. The high flow speed ($Re{\sim}1700$) maintained the shape of bent twines, and as the flow speed decreased, the model slightly deflated.
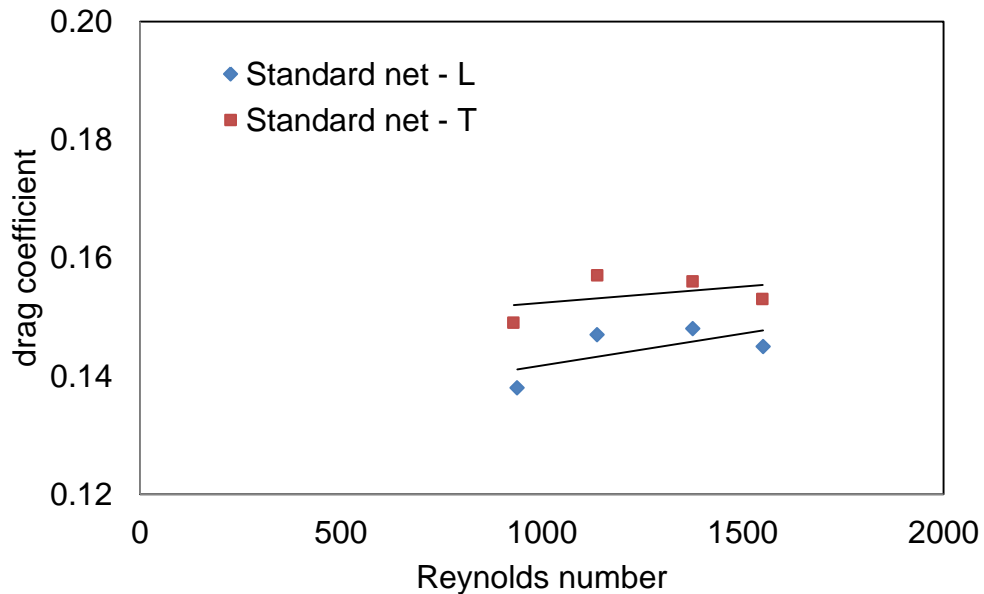
Fig. 4.16 Drag coefficient with respect to Reynolds number.
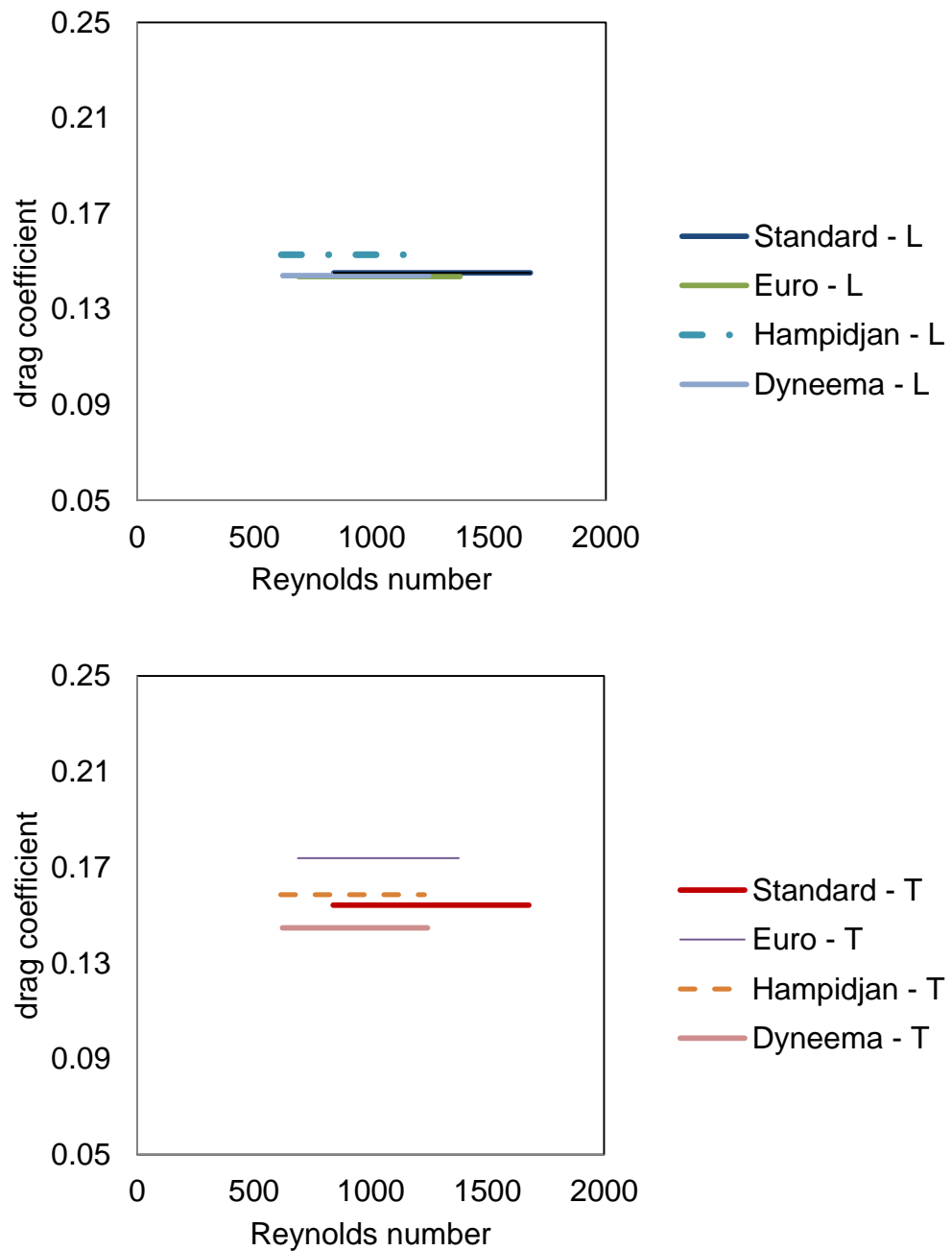
Fig. 4,17 The drag coefficient variation with respect to Reynolds number – linear regression analysis applied to standardise trawl inflation.

A drag increase due to inflation was 6%. A linear regression analysis was done to standardise slight changes in the drag coefficient due to the model inflation, and the results are shown in Fig. 4.17. For the longitudinal stretch, the drag coefficient for

all models except Hampidjan collapse on one trend line. The exception of Hampidjan from the general trend could be explained by the following two reasons:

(1) The effect of Hampidjan material double-knot was not fully captured by accounting for the size of the knot in to the twine area. The double knot due to its increased size and, for this reason, an amplified irregularity of its shape (compared to a single knot) caused significant changes in the way the boundary layer separated.

(2) The double knot, as shown in chapter 3, significantly restrained a lateral mesh opening of the netting, which limited an extent of twine bending from applying the pre-stretch process.

Net drag coefficient at a low angle of attack

As discussed in section 1.5, for the nets exposed to the flow at a low angle of attack, previously-published results show inconsistency in the way the Reynolds number, netting porosity and a low angle of incident flow affect the drag coefficient. The drag coefficient from the longitudinally pre-stretched models was used in this study to compare the figures against previous results. Fig. 4.18 summarizes the results of some previous works and the present study. Empirical formulae for the drag coefficient of plane nets in a steady current as a function of angle of attack and net solidity established by Aarsnes et al. (1990) is not included in Fig. 4.18 as the formulae assumed a constant Reynolds number. The experimental results from Taniguchi (1968) showed that the drag of a conical shape net that produced an angle to the incident flow of 12^0 depended strongly on the Reynolds number. However, the drag values were over 1.5 – as these values are well-above the results of similar studies shown on Fig 4.18, Taniguchi's data is not shown in Fig. 4.18 for illustrative purposes. Dvernik (1971) based on experimental results approximated the drag coefficient as a linear function of the angle of attack between 6^0 and 14^0, and $10^3 < Re < 10^4$. In general, the results of this study agree with Dvernik's work that the drag coefficient is independent of the Reynolds number. However, an application of his formula for a weighted average angle of attack of 9.8^0 (which was a case for the present study) suggest a drag coefficient value significantly greater than was found

in this study. The results of Buxton &DeAlteris (1992) suggest that for the drag coefficient at a low angle of attack is dependent on the Reynolds number for Re<1000. A similar effect of the Reynolds number on the drag coefficient is shown by Gjøsund & Enerhaug (2010).
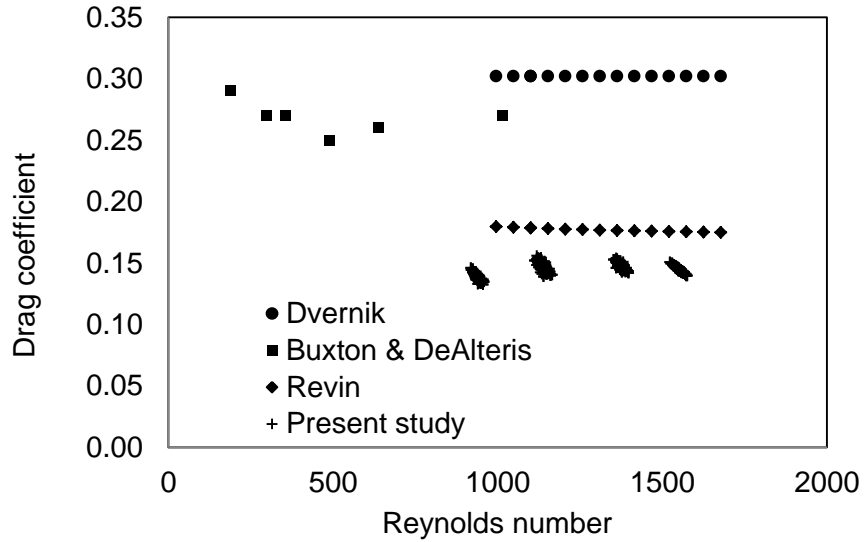
Fig. 4.18 Drag coefficient with respect to Reynolds number – various study comparison.

Revin (1959) proposed an approximation for the drag coefficient for the plane net at an angle of attack $C_{d[net]}^{\propto}$:

$$C_{d[net]}^{\propto} = C_{d[net]}^{0} + [C_{d[net]}^{0} + C_{d[net]}^{90}]\frac{\propto}{90^0}$$

4.7

where $C_{d[net]}^{o}$ and $C_{d[net]}^{\propto 90}$ are the drag coefficient for the plane net parallel and perpendicular to the flow, respectively.

The drag coefficient for the plane net sheet at 90^0 to the flow can be estimated from eq. 4.6 (Balash et al. 2009) as a function of the drag coefficient for a cylinder (eq. 4.7) modified by a function of net blockage.

$$C_{d[net]} = C_{d[cyl]}(8.03S_d^2 - 0.74S_d + 0.12)$$

4.8

$$C_{d[cyl]} = 1 + \frac{10}{Re^{2/3}} \qquad\qquad 4.9$$

The drag coefficient for the plane net parallel to the flow $C_{d[net]}^{o}$ was calculated applying the Konogaya & Kawakami (1971) approximation based on experimental results:

$$C_{d[net]}^{o} = 0.37\frac{d}{m} - 0.58\left(\frac{d}{m}\right)^{3/2} \qquad\qquad 4.10$$

where *d* is twine thickness and *m* is a mesh bar.

As can be seen from Fig. 4.18, Revin's approximation (1959) is the most accurate among the considered methods proving a prediction value of 9% greater than the drag coefficient found in this study.

Wakeford (1994) measured the drag force on four 2 fathom prawn trawl models at flow velocity of 0.75m/s over a range of spread ratios between 40% and 95%. All models were of an equivalent number of meshes deep, but wing taper sequences varied between the models. For the model with typical wing tapers (similar to the present study case), the drag coefficient varied by about 20% with respect to the horizontal spread range most commonly employed by the industry (70-85%).The drag coefficient in Wakeford's experiments was found to be greater compared to the present study. Where the vertical trawl opening was fixed with struts equally spaced along the trawl mouth and may have kept relatively low the degree to which twine area was exposed to the flow. Wakeford also simulated a bulk of fish collected in the cod-end, which would have increased the total measured drag to some degree. Wakeford (1994) conducted his experiments for a constant Reynolds number (about 433). The data from the studies of Buxton & DeAlteris (1993) and Gjøsund & Enerhaug (2010) suggest a higher drag coefficient for nets with Reynolds number below 10^{3} due to a pronounced relation between the drag coefficient and *Re<103,* a drag coefficient difference between Wakeford (1994) and current study could be

further explained by a difference in Reynolds numbers between the two prawn trawl studies.

Chapter 5
Conclusions

This chapter summarises the main work and findings of the thesis, highlights the implications of the research and identifies future work in the area.

5.1 Summary

Prawn net flexural rigidity

A novel experimental technique was developed to quantify net stiffness for fishing nets. Applying this technique, flexural rigidity figures were estimated for four full-scale prawn trawl net materials that are commonly used by prawn trawlers in Australia. The results indicate that a previously-suggested linear relationship between flexural rigidity and linear twine density is not applicable for cases of low linear density. Further experimentation is required to robustly define flexural rigidity as a function of linear density – this predictive tool will progress research on implications of fishing net stiffness that concern trawl drag and fishing gear selectivity.

Prawn trawl drag due to flexural rigidity

Prawn trawl models built from the netting being assessed for flexural rigidity were tested in the flume tank with respect to their drag and shape over a range of flow velocities. To quantify the effect of flexural rigidity on drag, each trawl was pre-

stretched longitudinally and transversely respectively before measuring the drag from two independent tests in the flume tank. The trawl model pre-stretch technique was shown to be an efficient and consistent method (with an error less than 0.5%) for standardising the effect of flexural rigidity on drag. The drag was found to be strongly and non-linearly affected by flexural rigidity: an increase of the flexural rigidity by 16% caused the drag increase of 7% and an increase of the flexural rigidity by 19% lead to the drag being increased by 20%. The results also showed that the drag coefficient for prawn trawls was weakly dependent on the Reynolds number in the typical for prawn trawls flow regimes of 1000<*Re<1700*. In addition, a double-knot material has demonstrated a strong mesh opening resistance which caused a drag increase of 10% compared to knotless or single knotted materials. A limited longitudinal mesh opening caused by double knots may also have serious selectivity implications as chances for non-targeted species to escape the trawl would be reduced.

Prawn trawl shape due to flexural rigidity

The physical trawl model was analysed in a simplified way as a system of independent plane net sheets, each with an orientation to the flow estimated from analysis of stereo-vision data. The weighted-average angle of incident flow was 9.8^{0} for all the models pre-stretched longitudinally with an exception of the double-knot model. In the case of transverse pre-stretch, which showed an extent of global (overall shape) deformation, the angle increased by 5% for the models built from stiff materials. Previous research data on prawn trawl drag variation with respect to spread ratio was also utilised to estimate the relationship between drag coefficient and net-sheet orientation. The drag varied significantly with respect to the horizontal spread within the most commonly employed by the industry range of 70-85%.

5.2 Implications of research

This research has developed practical methodologies to advance the knowledge of fishing net hydrodynamics:

1. The work shows that full-scale netting can be effectively used in flume tank experiments on model trawls provided flexural rigidity is standardized. Flexural rigidity standardisation is achieved through a longitudinal pre-stretch process. With the method applied, the drag coefficient for trawl models built from stiff netting materials was equal to that of soft material.

   The use of full-scale netting has the following advantages for the testing of trawls in the flume tank:

   - The effect of twine rigidity is intrinsically incorporated into the experiment by applying a standardised pre-stretch process to the model trawls during testing.
   - As shown in this study, the drag coefficient for model prawn trawls is independent of the small associated change in the Reynolds number. In the case of mid-water trawls however, the drag coefficient is affected by the large change in the Reynolds number. Dynamic and geometric similarity between the full-scale trawl and the tested model-trawl often cannot be achieved simultaneously due to practical limitations. This shortcoming results in significant drag over prediction (by up to 70%). Full-scale material usage for building model trawls provides significantly improved scale estimates as drag results for the model and prototype correspond to a similar Reynolds number based on twine diameter.
   - When full-scale netting is used to build model trawls, net solidity (a ratio of twine area to the area covered by the net) is maintained constant between the model and prototype. When model netting is

used, it is often impossible to scale down twine diameter and mesh size proportionally, which results in net solidity being different between the model and prototype, and hence leads to additional scaling errors.

- Time and cost efficiency is considerably increased because models built from full-scale material require significantly less human resources and financial investments. Full-scale nets are easily available compared to the model netting material, and model netting due its fineness is also significantly more time-consuming to build models from.

The limitation of full-scale material usage is that models may not be accurately tested at low speed as the flow would not be strong enough to overcome netting buoyancy.

2. The net pre-stretch process has been shown to affect model drag by up to 20%. The technique may be applied in commercial operations to minimise drag, but the size of the effect cannot be accurately estimated by the current flume tank data. The technique requires some labour and time input depending on the size of the full-scale prawn trawl. Successful application could provide significant fuel savings. However, the relative effect of the pre-stretch on full-scale trawl shape is limited to areas where netting tension is low: cod-end and in areas down the side of the trawl.

3. A stereo-vision system developed in this work can be employed to accurately capture the shape of the trawl and mesh opening, and allow analysis in connection with the generation of drag and improved catch selectivity.

Mixed results have been previously reported on the drag coefficient for low porosity nets exposed to the flow at a low angle of attack This study, in application to the

prawn trawl, examined an extent by which the Reynolds number, and an angle of incident flow determine the drag coefficient. The prawn trawl drag coefficient is generally independent of the Reynolds number above 10^3. Based on a previous study, the drag coefficient can also be said to vary significantly with respect to the horizontal spread within the range most commonly employed by the industry of 70-85%. These findings combined imply that net drag needs to be estimated using a process involving trawl twine area, towing speed, and spread ratio in application to prawn trawling systems.

Hampidjan material would provide a significantly better low-drag performance if single knots instead of double knots were used by the manufacture. Knot stability is only marginally improved by using a double-knot, but returns very limited practical benefits.

5.3 Recommendations for future work

Further testing of assorted fish and prawn nets with respect to flexural rigidity will create an increasingly powerful set of data to robustly define the relationship between netting flexural rigidity and linear twine density. This will allow estimating net flexural rigidity with a predictive tool (formula) in future research that concerns net stiffness.

Extensive data on drag vs. trawl shape for various trawl designs can be collected with the stereo-vision system and explored by conceptualising the trawl as plane net sheets exposed to the free-stream at certain angles. This data can be used to calibrate an associated drag prediction system for prawn trawls, including new prawn trawl designs.

The softness of Dyneema® material, which is due to its multi-filament structure and small overall diameter, is said to produce unwanted complications during trawling operations. In addition to the significantly higher cost of Dyneema® compared to conventional materials, the softness factor is one of the reasons the industry has

been reluctant to widely implement the innovation. The issue may be overcome if the material's stiffness is increased with a chemical or heat treatment. Firstly, the extent and process by which different levels of stiffness affect prawn trawl drag needs to be quantified in the flume tank; followed by sea-trials where an optimal stiffness and operating procedure may be determined that mitigates the practical difficulties being experienced while maintaining low drag.

References

ABARE 2008, *Fishers Reeling as Exchange Rate and Fuel Prices Bite*.

Andreyev, NN 1960, 'Uravnenie Poverkhnosti Setnogo Polotna, Prikreplennogo k Dvum Obrucham [in Russian]', *Trudy Kaliningradrybvtuza*, vol. 11, pp. 15-28.

Baranov, FI 1960, *Tehnika Promyshlennogo Rybolovstva* Pishchepromizdat.

Brandt, A & Carrothers, PJG 1964, 'Test Methods for Fishing Gear Materials', *Mod. Fishing Gear of the World*, vol. 2, pp. 9-49.

Chow, YS 1969, 'Studies on Scale Range of Applicability of Model Tests', *Journal of Agricultural Association*, vol. 68, pp. 56-63.

Christensen, BA 1975, 'Hydrodynamic Modelling of Fishing Nets', *IEEE Ocean*, pp. 484-490.

Clark, M 2006, *Wild-catch Prawn Industry of Australia Situation Assessment, Challenges and Opportunities, a Strategic Path Forward. Executive Summary*, <http://www.prawncouncil.com.au/publications.html >.

Dickson, W 1961, 'A Study Relating Models to Commercial Trawls', *Mar. Res. Dep. Agric. Fish. Scotl.*, vol. 1, pp. 1-48.

Fiorenti, L, Sala, A, Hansen, K, Cosmi, G & Palumbo, V 2004, 'Comparison Between Model Testing and Full-scale Trails of New Trawl Design for Italian Bottom Fisheries', *Fisheries Science*, vol. 70, pp. 349-359.

Flesser, C 1994, 'Evaluating Florida Flyer Net Perfomance with Selvage Tapers of 1N2B, 1N3B and 1N4B', B.Sc. thesis, Australian Maritime College.

Fonteyne, R, Buglioni, G, Leonori, I & O'Neill, FG 2007, 'Review of Mesh Measurement Methodologies', *Fisheries Research*, vol. 85, no. 3, pp. 279-284.

FRDC 2005, *Fishery Research Development Corporation (FRDC) Workshop*.

FRDC 2007, 'Higher Prices Fuel the Need for Greater Efficiency', *Fishery Research Development Corporation media realise*, vol. 16, no. 14.

FRDC 2008, *Higher Prices Fuel the Need for Greater Efficiency*, Fisheries Research Development Corporation.

Fredsøe, J & Sumer, BM 1997, *Hydrodynamics Around Cylindrical Structures*, Advanced series on ocean engineering ; v. 12, World Scientific, Singapore ; River Edge, NJ.

Fridman 1986, *Calculations for Fishing Gear Designs*, FAO fishing manuals, Published by arrangement with the Food and Agriculture Organization of the United Nations by Fishing News, Farnham.

Fridman, AL 1973, *Theory and Design of Commercial Fishing gear*, Israel Program for Scientific Translations, Jerusalem,.

Gjøsund, SH & Enerhaug, B 2010, 'Flow through nets and trawls of low porosity', *Ocean Engineering*, vol. 37, no. 4, pp. 345-354.

Hu., F, Matuda, K & Tokai, T 2001, 'Effects of Drag Coefficient of Netting For Dynamic Similarity on Model Testing of Trawl Nets', *Fisheries Science*, vol. 67, pp. 84-89.

JCFA 1964, 'Fishing Gear of the World', in *Seconcd FAO World Fishing Gear Congress*, London, vol. 2.

Klust, G 1982, *Netting materials for fishing gear*, FAO fishing manuals, Fishing News for the Food and Agriculture Organisation, West Byfleet.

Kok, SE 2010, 'Improving Flow Quality of the Flume Tank Using Experimental Results', B.Eng thesis, University of Tasmania.

Lowe, T 1996, 'An Analysis of the Gains in Engineering Performance Achieved by Constructing Australian Prawn Trawls from Spectra Netting', B.Sc. thesis, Australian Maritime College.

Lowry, N & Robertson, JHB 1996, 'The Effect of Twine Thickness on Cod-end Selectivity of Trawls for Haddock in the North Sea', *Fisheries Research*, vol. 26, no. 3-4, pp. 353-363.

Milne, PH 1979, *Fish and Shellfish Farming in Coastal Waters*, Fishing News Books Ltd, England.

O'Neill, FG 2003, 'A Theoretical Study of the Factors Which Influence the Measurement of Fishing Netting Mesh Size', *Ocean Engineering*, vol. 30, no. 16, pp. 2053-2063.

O'Neill, FG & Priour, D 2009, 'Comparision and validation of two models of netting deformation', *Journal of Applied Mechanics*, vol. 76, no. September

O'Neill, FG 1997, 'Differential Equations Governing the Geometry of a Dimond Mesh Cod-end of a Trawl Net', *Journal of Applied Mechanics*, vol. 64, pp. 1631-1648.

O'Neill, FG 2002, 'Bending of Twines and Fibres Under Tension', *Journal of the Textile Institute*, vol. 93, no. 1-1.

Otsu, N 1979, 'A Threhold Selection Method for Grey-level Histograms', *IEEE Transactions of Systems, Man and Cybernetics*, vol. 9, no. 1, pp. 62-66.

Priour, D 2001, 'Introduction of Mesh Resistance to Opening in a Triangular Element for Calculation of Nets by the Finite Element Method', *Commun. Numer. Meth. Engng*, vol. 17, pp. 229-237.

Priour, D & Cognard, J-Y 2011, 'Investigation of methods for the assesment of the flexural stifness of netting panels', in *DEMAT*, Split, Croatia, pp. 203-219.

Revin, AS 1959, 'Issledovanie Vliyaniya Structury i Formy Tralovoi Seti na ee Soprotivlenie v Potoke Vody [in Russian]', *Trudy VNIRO*, no. 41.

Rozenshtein, MM 2000, *Mehanika Orudiy Rybolovstva [in Russian]*, Kaliningrad State Technical University Press.

Sala, A, O'Neill, FG, Buglioni, G, Lucchetti, A, Palumbo, V & Fryer, RJ 2007, 'Experimental Method for Quantifying Resistance to the Opening of Netting Panels', *ICES Journal of Marine Science*, vol. 64, pp. 1573-1578.

Sterling 1998, 'The Improvement of Prawn Trawling Perfomance Through Analysis of Ottter Board Design and Operation', Masters thesis, Curtin University of Technology.

Sterling & Eayrs 2010, 'Trawl-gear Innovations to Improve the Energy Efficiency of Australian Prawn Trawling', paper presented to 1-st International Symposium in Fishing Vessel Energy Efficiency, Vigo, Spain, May 2010.

Sterling, D 1996, *Abridged Description and Performance Appraisal of Australian Prawn Trawl Systems*, D.J. Sterling Trawl Gear Services, Tin Can Bay, Queensland.

FRDC 2007, *Fishing Energy Efficiency Review for the FRDC*, 2005/239.

Tait, D 1987, *The Effect of Knotless and Knotted Netting on the Drag of Demersal Trawl Nets*, Nova Scotia, Canada.

Tauti, M 1934, 'A Relation between Experiments on Model and on Full-scale of Fishing Net', *Nippon Suisan Gakkaishi*, vol. 3, pp. 171-177.

Tsukrov, I, Drach, A, DeCew, J, Robinson Swift, M & Celikkol, B 2011, 'Characterization of geometry and normal drag coefficients of copper nets', *Ocean Engineering*, vol. 38, no. 17–18, pp. 1979-1988.

Wakeford, J 1994, *The Effect of Frameline Tapers on the Engineering Perfomance of Prawn Trawl Systems*, Australian Maritime College, Launceston.

Watson, JW, Workman, IK, Taylor, CW & Serra, AF 1984, *Configurations and Relative Efficiencies of Shrimp Trawls Employed in Southern United States Waters*, National Maritime Fisheries Services, NOAA.

Weszka, JS & Rozenfeld, A 1978, 'Threhold Evaluation Technique', *IEEE Transactions of Systems, Man and Cybernetics*, vol. 8, no. 8, pp. 622-629.

White, FM 1974, *Viscous fluid flow*, McGraw-Hill, New York.

Wray, T 1990, 'Y-design Trawl Keeps Meshes Open: New Concept Gear Lets Small Fish Escape', *Fish. News*, no. 3976:10–11.

Appendix I

Numerical solution for estimating the shape of the restrained between two hoops

The shape of the net restrained between two hoops according to Andreyev (1960) is determined with the following equation:

$$\int_0^x dx = \frac{1}{k}\left[\int_{\pi/2}^{\varphi}\sqrt{1-c_1\sin^2\varphi}\,d\varphi - \int_{\pi/2}^{\varphi}\frac{1}{\sqrt{1-c_1\sin^2\varphi}}\,d\varphi\right] \qquad \text{A1}$$

where

$$c_1 = 1 - u_0^2$$

$$k = \frac{u_y}{y}$$

u_0 is the hanging coefficient in the middle section between the hoops

$$z = \cos\phi \quad \text{and} \quad d\phi = \frac{\sqrt{1-\sin^2\varphi}}{\sqrt{\frac{1}{c_1}-\sin^2\varphi}}\,d\varphi$$
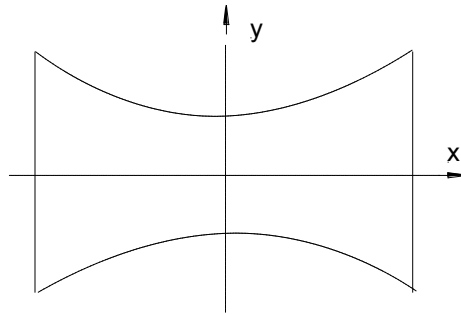

Fig. A1 Axis specification.

Then, integrating the eq. A1:

$$kx = -\int_o^{\pi/2}\sqrt{1-c_1\sin^2\varphi}\,d\varphi + \int_0^{\pi/2}\frac{d\varphi}{\sqrt{1-c_1\sin^2\varphi}} + \int_o^{\varphi}\sqrt{1-c_1\sin^2\varphi}\,d\varphi - \int_0^{\varphi}\frac{d\varphi}{\sqrt{1-c_1\sin^2\varphi}}$$

Matlab code to solve the governing equations in order to estimate the length between the hoops:

```
nseg = 10
U0 = 0.215; hanging coefficient in the middle (narrowest) section
R1 = 0.582; hanging coefficient on the hoop
r=.190; hoop radius
C1=1-U0^2;
dphi = pi/1000

dif = R1-U0
du = dif/nseg

u = R1
temp_sinphi = (1-u.^2)./(1-U0.^2)

phix = asin(temp_sinphi)

% creating the vector of 0 to pi/2
vphi01 = 0:dphi:pi/2
vphi02 = 0:dphi:phix

%% numerical integration step-1
phSQ01a = (1-C1.*sin(vphi01).*sin(vphi01)).^0.5;
phSQ01b = 1./phSQ01a;

phSQ02a = (1-C1.*sin(vphi02).*sin(vphi02)).^0.5;
phSQ02b = 1./phSQ02a;

%   see the results
figure(1)
clf
subplot(4,1,1)
plot(vphi01,phSQ01a)
title('phSQ01a')

subplot(4,1,2)
plot(vphi01,phSQ01b)
title('phSQ01b')

subplot(4,1,3)
plot(vphi02,phSQ02a)
title('phSQ02a')

subplot(4,1,4)
plot(vphi02,phSQ02b)
title('phSQ02b')

%% numerical integration step-2
Z01a = trapz(vphi01,phSQ01a);
Z01b = trapz(vphi01,phSQ01b);
Z02a = trapz(vphi02,phSQ02a);
```

```
Z02b = trapz(vphi02,phSQ02b);
disp(' =========================')
disp('  ')
disp(' Answer ')
disp(' Answer ')
disp(' Answer ')
L_net = (- Z01a + Z01b  + Z02a - Z02b)*2*r/R1

disp([' Length of Net is ',num2str(L_net,5),'m'])
```

Appendix II

Calibration frame
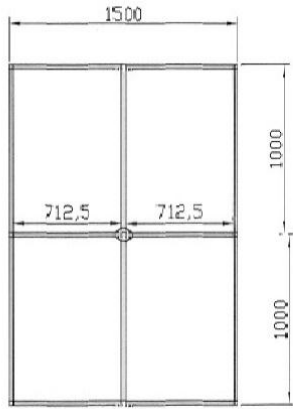
View Top

View Right

View Front